4 SCIENTIFIC HIGHLIGHT OF THE MONTH

First-principles design of magnetic oxides

A. Ernst[1], G. Fischer[2], P. Buczek[1], S. Ostanin[1], M. Däne[3], I. V. Maznichenko[2], A. Marmodoro[1], M. Hoffmann[1,2], W. Hergert[2], L. V. Bekenov[4], V. N. Antonov[1,4], I. Mertig[1,2], J. B. Staunton[5], N. Sanchez[6], M. C. Muñoz[6], M. Lüders[7], L. Petit[7], Z. Szotek[7], and W. M. Temmerman[7]

[1] Max-Planck-Institut für Mikrostrukturphysik, Weinberg 2, D-06120 Halle, Germany
[2] Institut für Physik, Martin-Luther-Universität Halle-Wittenberg, D-06099 Halle, Germany
[3] Lawrence Livermore National Laboratory, USA
[4] Institute of Metal Physics, 36 Vernadsky Street, 03142 Kiev, Ukraine
[5] University of Warwick, Department of Physics, Coventry, CV4 7AL, United Kingdom
[6] Instituto de Ciencia de Materiales de Madrid, Consejo Superior de Investigaciones Científicas, Cantoblanco, 28049 Madrid, Spain
[7] Daresbury Laboratory, Daresbury, Warrington, WA4 4AD, United Kingdom

Abstract

We present an efficient methodology for the computational design of structural, electronic and magnetic properties of complex magnetic oxides. Our approach combines several complementary first-principles methods rooted in density functional theory. The optimization of atomic positions and the optimization of the crystalline structure is achieved by means of pseudopotential methods, known for yielding precise total energies and forces. The obtained structural information constitutes an input for calculations of electronic and magnetic properties using the Korringa-Kohn-Rostoker and Linear Muffin-Tin Orbital methods. The resulting Kohn-Sham Green function is utilized in various applications, including the description of transport, spectroscopic properties and magnetism. This *multi-code* approach is particularly well suited for strongly correlated systems and therefore enables a faithful description of complex oxides. In this highlight, we illustrate the strengths of the methodology on examples of electronic and magnetic properties of transition metal monoxides, diluted magnetic oxides and magnetic oxidic surfaces.

1 Introduction

In recent years magnetic oxides have attracted enormous interest due to a strong interplay between their charge and lattice degrees of freedom and magnetic properties. They appear promising for technological applications, especially in electronics, as most of them turn out to be insulators. The electronic and magnetic properties of oxides have been the subject of intense research over the last few years oriented towards synthesis of new materials with prescribed properties tuned by manipulation of composition and structure. This expanding experimental field has recently profited substantially from theoretical support. In particular, first-principles simulations of ground and excited state properties go hand-in-hand with experiments allowing interpretation of experimental results in these complex systems and providing additional insight into various properties of these materials. They also help to identify the technologically most promising systems, reducing the experimental burden.

First-principles simulations of real materials and the prediction of their chemical and physical properties remain one of the most ambitious aims of modern computational physics. Ground state properties of any electronic system can be in principle exactly determined within density functional theory (DFT) by Hohenberg and Kohn [1]. The most popular local spin density approximation (LSDA) [2] and the generalized gradient approximation (GGA) [3, 4] of the exchange-correlation functional enable an adequate parameter-free description of many realistic materials, especially systems with itinerant electrons. However, the LSDA and GGA fail to reproduce correctly ground state properties of systems with strongly or partially localized electrons. This is associated mainly with an unphysical self-interaction (SI) of an electron with itself [5], occurring in the Hartree term of the LSDA and GGA energy functionals on account of the local approximation applied to the exchange-correlation energy functional. Another difficulty for first-principles calculations is the correct description of excited state properties which is a fundamental problem of the static nature of DFT. While the band structure and spectral density can be approximately calculated for metals, DFT underestimates the size of the fundamental band gap in semiconductors and insulators by about 50-60%. Since many oxides are insulators and, in addition, may contain localized or partially localized electrons, first-principles simulations of these systems are difficult.

Nowadays one can resort to several formalisms going beyond the LSDA and GGA which can provide an adequate description of oxides. The spurious self-interaction can be subtracted for all localized orbitals using the self-interaction correction to LSDA method (SIC-LSDA) [5], established and widely used in computational chemistry and physics. Electronic correlations can be in many cases efficiently modelled using the LDA+U method [6], in which a Hubbard term with the on-site Coulomb interaction U is added to the LSDA functional to give a better account of the Coulomb interaction between electrons. In many cases, U is an adjustable parameter, which is chosen to optimize agreement with experiment. The so-called double counting term is an additional shortcoming of the LDA+U approach. Besides LDA+U and SIC-LSDA schemes, a class of hybrid functionals has recently been introduced [7]. These functionals treat Coulomb correlations beyond the LSDA, accomplished by incorporating some fraction of the exact exchange. Excited state properties can be studied within the GW approximation, which provides a self-energy and a one-electron Green function, alas practically always resorting to the random-phase approximation [8]. Despite its enormous merit in semiconductor physics, this method is not very suitable for complex oxides, since, firstly, it is still numerically very demanding and time consuming, and, secondly, the random phase approximation is valid only for weakly correlated systems. Another method to calculate excitations is dynamical mean-field theory (DMFT), which is especially designed for strongly correlated materials and allows for local dynamical correlations to be systematically included into lattice models [9]. However, most applications to date invoke the Hubbard Hamiltonian, via the so-called LDA+DMFT implementation, and thus inherit the uncertainties associated with the LDA+U method.

In this highlight we overview our approach to the first-principles description of complex oxides focusing, in particular, on their magnetic properties. This approach is based on a Green function method, providing access to the magnetic susceptibility and excited state properties, e.g. spin-waves. The key quantity of this approach, the one-electron Kohn-Sham Green's function, can be efficiently calculated for large complex systems within multiple scattering theory using the Korringa-Kohn-Rostoker (KKR) [10, 11] and the Linear Muffin-Tin Orbital (LMTO) [12] implementations. The crystal structures of the studied oxides can be obtained either from experiment or from first-principles simulations using pseudopotential methods, which are known to provide precise total energies and forces. This *multi-code* approach is presented in the next section 2. Then, in sections 3 and 4 respectively, we discuss magnetic properties of the bulk transition metal monoxides and diluted magnetic oxides. Section 5 deals with exotic magnetic surfaces of nonmagnetic oxides, and conclusions are in section 6.

2 Methodology

The key input for any theoretical analysis is the electronic spectrum. In our approach it is given by the one-electron Kohn-Sham Green function which in real space is represented in terms of a complete set of orthonormal wavefunctions, $\psi_i(\mathbf{r})$, the eigenfunctions of a Kohn-Sham Hamiltonian, and corresponding eigenenergies ε_i

$$G(\mathbf{r},\mathbf{r}';E) = \sum_i \frac{\psi_i(\mathbf{r})\psi_i^*(\mathbf{r}')}{E-\varepsilon_i}\,. \tag{1}$$

The Green function (1) can be also found as the resolvent of the Kohn-Sham equation avoiding calculations of the Kohn-Sham eigensystem

$$(-\nabla^2 + V(\mathbf{r}) - E)G(\mathbf{r},\mathbf{r}';E) = -\delta(\mathbf{r},\mathbf{r}')\,. \tag{2}$$

Above, $V(\mathbf{r})$ is an effective Kohn-Sham potential. Eq. (1) can be solved self-consistently within the density functional theory for any arrangement of atoms. Within the multiple scattering theory [13], the Green function can be directly constructed for any complex energy.

Using the Green function (1), the expectation value of an observable $\hat{\mathcal{O}}$ can be straightforwardly calculated as

$$\langle\hat{\mathcal{O}}\rangle = -\frac{1}{\pi}\mathrm{Im}\,\mathrm{Sp}\int_{-\infty}^{+\infty} dE\, f(E)\hat{\mathcal{O}}G(\mathbf{r},\mathbf{r}';E)\,, \tag{3}$$

where $f(E)$ is the Fermi-Dirac distribution function.

The fundamental advantage of working with Green's functions is the possibility to evaluate readily the properties of a perturbed system by resorting to the Dyson equation

$$G(\mathbf{r},\mathbf{r}';E) = G_0(\mathbf{r},\mathbf{r}';E) + \int d\mathbf{r}''\, G_0(\mathbf{r},\mathbf{r}'';E)\Delta V(\mathbf{r}'')G(\mathbf{r}'',\mathbf{r}';E)\,, \tag{4}$$

where $G_0(\mathbf{r},\mathbf{r}';E)$ is the Green function of an unperturbed system and $\Delta V(\mathbf{r}')$ is the perturbation.

According to Eqs. (3,4) the expectation value of an observable $\hat{\mathcal{O}}$ for the perturbed system can be expressed in the linear response formalism as

$$\langle\hat{\mathcal{O}}\rangle = -\frac{1}{\pi}\mathrm{Im\,Sp}\int\limits_{-\infty}^{+\infty} dE\, f(E)\left[\hat{\mathcal{O}}G_0(\mathbf{r},\mathbf{r}';E) + \int d\mathbf{r}''\,\hat{\mathcal{O}}G_0(\mathbf{r},\mathbf{r}'';E)\Delta V(\mathbf{r}'')G_0(\mathbf{r}'',\mathbf{r}';E)\right]. \quad (5)$$

The single particle Green's function given by the Dyson equation (4) suffices to describe the effects of *static* perturbations on the system of interest. When the perturbing potential varies in time, the evolution of the system properties can be found from the time dependent density functional theory [14]. When the coupling to the external field is weak one can resort to the linear response time dependent density functional theory [15] to find the first order time variations of the charge and magnetization densities. The response is completely determined by the ground state properties of the unperturbed ensemble which simplifies considerably the formalism and reduces the numerical effort. Physically, the linear response theory provides a picture of "natural" excitations and fluctuations of the system [16, 17]. Formally, the calculations involve two steps, leading to a two-particle Green's function, i.e. the dynamic susceptibility of the system [18].

First, one considers the *Kohn-Sham susceptibility*

$$\chi^{ij}_{\mathrm{KS}}(\mathbf{x},\mathbf{x}',\omega) = \sum_{km}\sigma^i_{\alpha\beta}\sigma^j_{\gamma\delta}(f_k - f_m)\frac{\psi_k(\mathbf{x}\alpha)^*\psi_m(\mathbf{x}\beta)\psi_m(\mathbf{x}'\gamma)^*\psi_k(\mathbf{x}'\delta)}{\omega + (\varepsilon_k - \varepsilon_m) + \mathrm{i}0^+}, \quad (6)$$

giving the retarded response of the formally non-interacting Kohn-Sham system. The 0^+ notation is introduced to stress that we deal with retarded quantities. $f_j \equiv f(\epsilon_j)$ is the occupation of state j. $\sigma^{0,x,y,z}_{\alpha\beta}$ are standard Pauli matrices associated with the charge and magnetization. The induced charge and magnetization densities described by the Kohn-Sham susceptibility modify the Hartree and exchange-correlation potential, giving rise to a self-consistent problem: the induced densities contribute to the effective fields and are, simultaneously, induced by it. The self-consistency is reflected in the second step of the formalism

$$\begin{aligned}\chi^{ij}(\mathbf{x},\mathbf{x}',\omega) = {}& \chi^{ij}_{\mathrm{KS}}(\mathbf{x},\mathbf{x}',\omega) + \\ & \sum_{k,l=0}^{3}\iint d\mathbf{x}_1 d\mathbf{x}_2\chi^{ik}_{\mathrm{KS}}(\mathbf{x},\mathbf{x}_1,\omega)\left(K^{kl}_{\mathrm{xc}}(\mathbf{x}_1,\mathbf{x}_2,\omega) + \frac{2\delta_{k0}\delta_{l0}}{|\mathbf{x}_1-\mathbf{x}_2|}\right)\chi^{lj}(\mathbf{x}_2,\mathbf{x}',\omega).\end{aligned} \quad (7)$$

The last equation is referred to as "susceptibility Dyson equation", because of its characteristic form. χ is the density-density response function of the system and describes charge neutral excitations. It is often termed the *enhanced susceptibility*. The exchange-correlation kernel, K_{xc}, is defined as a functional derivative of an exchange-correlation potential with respect to the density

$$K^{ij}_{\mathrm{xc}}[\langle\boldsymbol{\hat\sigma}(\mathbf{x})\rangle](\mathbf{x},\mathbf{x}',t-t') = \frac{\delta v^i_{\mathrm{xc}}(\mathbf{x},t)}{\delta n^j(\mathbf{x}'t')} \quad (8)$$

evaluated at the ground state values of electronic and magnetic densities.

The enhanced susceptibility provides us with the spectrum of excited states of the system. The spin excitations are particularly relevant for the determination of magnetic properties of materials. For instance, the critical temperatures of magnetic transitions (Curie and Néel points) crucially depend on the spin excitations.

The static magnetic susceptibility $\chi(\mathbf{q})$ can be used to determine the magnetic ordering in which the system stabilizes below the critical (Curie or Néel) temperature T_c. The paramagnetic state above T_c can be modelled using the disordered local moment (DLM) [19, 20] picture, in which moments of different directions are assumed to form an alloy and are described within the coherent potential approximation [19, 20]. Subsequently, one evaluates $\chi(\mathbf{q})$ [21–23] which typically features a strong peak at the point in the Brillouin zone corresponding to the wave vector associated with the magnetic order below T_c. A substantial strength of the method is that it captures more correctly the electronic and magnetic properties of the system at elevated temperatures corresponding to the magnetic phase transition which might differ substantially from the ones evaluated at the absolute zero temperature for a fully ordered system.

The transverse magnetic fluctuations (spin-waves) can be also approximately described by means of *an adiabatic* treatment of the magnetic degrees of freedom [24, 25] where one maps the spin system onto an effective Heisenberg Hamiltonian of atomic moments which is much easier to implement. These adiabatic methods utilize density functional theory and, therefore, do not involve adjustable parameters. In this approach the existence of the single particle Stoner excitations is neglected, but they play no role in insulating materials which are the topic of this highlight.

The Heisenberg Hamiltonian reads

$$\mathcal{H} = -\frac{1}{2}\sum_{pr} J_{pr}\mathbf{e}_p \cdot \mathbf{e}_r, \tag{9}$$

where $\mathbf{e}_p \equiv \mathbf{S}_p/S_p$ ($\mathbf{S}_p$ is the ground state magnetic moment, S_p is the size of the moment and is always positive) and J_{pr} are the so-called exchange parameters. (We adopt a convention that $J_{pp} = 0$.) One proceeds now as follows. First, one extracts the effective coupling constants J_{pr} from an *ab initio* band structure calculation and in a second step Hamiltonian (9) is used to study magnetization dynamics and thermodynamics, including the determination of the spin-wave dispersion relation, the transition temperature, etc.

There are several computational schemes taking advantage of the outlined adiabatic spin dynamics. Using the so-called *magnetic force theorem* [26] one can determine directly the exchange parameters J_{pr} using the Green function method:

$$J_{pr} = \frac{1}{\pi}\int_{\infty}^{E_F} dE \int d\mathbf{r}_p \int d\mathbf{r}'_r B_{xc}(\mathbf{r}_p) G(\mathbf{r}_p, \mathbf{r}'_r; E) B_{xc}(\mathbf{r}'_r) G(\mathbf{r}'_r, \mathbf{r}_p; E)\,, \tag{10}$$

where E_F is the Fermi level, $B_{xc}(\mathbf{r})$ is the exchange-correlation magnetic field, and $G(\mathbf{r}, \mathbf{r}'; E)$ is the retarded Green function. Another method, the *frozen magnon approach* is a formally equivalent technique allowing to find directly the energies of different magnetic configurations [27]. The matrix J_{pr} can be also extracted from the knowledge of the *static* magnetic susceptibility [28].

In the collinear systems the excited states of the Heisenberg Hamiltonian are spin-waves under the assumption of small deviation of the moments from their ground state directions. Their spectrum and the corresponding transverse magnetization deviations are given as the eigensystem of the torque matrix associated with the Heisenberg Hamiltonian

$$\omega_\lambda e^+_{\lambda p} = \sum_r T_{pr} e^+_{\lambda r}, \quad T_{pr} \equiv 2S_p^{-1} \delta_{pr} \sum_l J_{pl} e_l - 2S_p^{-1} e_p J_{pr}. \tag{11}$$

The index λ labels eigenvalues. $e^+_{\lambda p}$ are interpreted as the spin-wave mode amplitudes on different magnetic sites and ω_λ is the spin-wave frequency.

Many oxides contain localized d- or f-electrons and cannot be correctly described within the conventional local spin density approximation, which is designed for itinerant systems and cannot take into account a strong on-site Coulomb interaction. As already mentioned, the self-interaction corrected local spin density approximation [5] is a useful scheme for describing a static limit of these correlations. In particular, it can determine whether an electron is localized or delocalized, i.e. whether its orbital is a part of valence band or not. This leads to a determination of the number of valence states and a nominal valence [29], as demonstrated by numerous calculation on rare earth, actinides, transition metal oxides (TMO), including the parent compounds of the high T_c superconductors and materials exhibiting a colossal magnetoresistance.

The so-called full SIC-LSDA scheme is rather time consuming [30], due to repeated transformations from reciprocal space (**k**-space) to real space to evaluate the self-interaction correction potential and then back transformation to **k**-space to solve the band-structure problem. So far most applications of the full SIC formalism have been performed with the SIC-LMTO-ASA band-structure method [12, 31, 32]. Later we have introduced a numerically simpler scheme, the so-called local SIC (LSIC), [33] implemented in the multiple scattering KKR code, which has opened up a new range of applications via its use of an alloy analogy and the coherent potential approximation (CPA), where a description of valence and spin fluctuations is warranted. The LSIC is based on the observation that more than 98% of the electron is localized on a site under consideration. In the vernacular of scattering theory a localized state is characterized by a very sharp resonance in its phase shift, associated with a large Wigner-delay time on that site. This allows us to use a single-site approximation, within multiple scattering theory, to determine the SIC charge density and potential. One of the advantages of the multiple-scattering implementation of the SIC formalism is that it can be easily generalized to include the coherent potential approximation, extending the range of applications to random alloys. In addition, one can use it to treat static correlation beyond the LSDA by studying pseudoalloys whose constituents are composed e.g. of two different states of a given system: one delocalized, described by the LSDA potential, and another localized, corresponding to the SIC-LSDA potential. Combined with the disordered local moment formalism for spin fluctuations [19, 20] to describe magnetic properties at finite temperatures, this also allows for different orientations of the local moments of the constituents involved.

A very important input for the determination of the electronic structure and its derived properties is the atomic structure, i.e. lattice constants, atomic positions, chemical composition, defects etc. We combine experimental and theoretical methods to access this information. A very valuable information is provided by XMCD experiments which we can fit to theoretical models using a fully relativistic LMTO band structure code [12, 34]. Additionally, structural properties can be extracted from LEED and x-ray diffraction (XRD) experiments [35]. On the theoretical side we resort to a multi-code approach. Several pseudopotential codes (e.g. VASP [36,37]) are used to relax the atomic positions by minimizing the total energy.

3 Transition metal monoxides

The $3d$ transition metal monoxides (TMO's) exhibit a rich variety of electronic and magnetic phenomena, and they justly have attracted a lot of attention over the last decades, in particular concerning the nature of the band gap and excitation spectrum in general. In the ground state the TMO's crystallize in the rock-salt structure and exhibit antiferromagnetic ordering of type 2 (AF II), with planes of opposite spins being repeated in alternating order along the [111] direction, defining two sublattices consisting of spin-up and spin down metal ions, respectively. The TMO's are Mott-Hubbard insulators (some of them are also of charge-transfer type) and belong to the class of strongly correlated systems. The origin of correlations in TMO's is a strong Coulomb-repulsion on the transition metal sites, which leads to localization of electrons and insulating behavior even though the d-bands are partially filled. Due to the highly correlated nature of the electron interaction in the TMO's, theoretical investigations employing first-principles methods to describe the electronic structure of these materials are difficult. The LSDA approximation fails to describe correctly certain properties of these oxides, predicting too small magnetic moments and gaps or even metallic behavior for CoO and FeO. Several approaches beyond the LSDA approximation have been applied for a realistic description of the TMO's. Among them is the LDA+U method [6], which achieves an effective Hubbard-splitting of d-bands using an effective Hubbard-U parameter. Another promising method appears to be the LDA+DMFT approach, which combines band structure and many-body theory, the dynamical mean field theory [9]. However, as mentioned earlier, these methods suffer from uncertainty of the external parameter U, which is difficult to obtain from first-principles, and the so-called double counting term. In contrast to these methods, the SIC-LSDA approach provides indeed a parameter free ab-initio description for the electronic structure of the TMO's. Several investigations of TMO's within the SIC approximation have been performed during the last decades [31,32,38–40]. Applying this approach to TMO's yields an improved electronic structure of these compounds which is then manifested in magnetic moments and band gaps, showing an adequate agreement with experiments. A significant finding is an explanation of how large insulating gap can persist into the paramagnetic state on account of disordered local moments.

3.1 Electronic structure

In our recent studies [38–40] we investigated electronic and magnetic properties of TMO's within the LSIC formalism [33]. One goal of these studies was to explore the consequences of applying LSIC to TMO's, since the LSIC is an approximation to the full SIC implementations. We found that the LSIC can describe trends for many physical properties of these compounds and compares well with full SIC implementations [31,32]. First of all, we performed total energy calculations for all possible valence configurations localizing particular electron $3d$-states by applying to these the self-interaction corrections. In agreement with other SIC calculations, we found the lowest total energy corresponding to the transition metal valence of 2^{+}, which corresponds to fulfiling the Hund's first rule, namely maximizing the spin moment. In the case of NiO, all d-electrons in one spin channel and 3 t_{2g} electrons in another spin channel are localized and have to be self-interaction corrected. The density of states of NiO, calculated within the LSIC-LSDA KKR method, is in good agreement with results, obtained with the full SIC-LSDA LMTO implementation (Fig.1). The same trend was found for the other compounds of the TMO series [39].

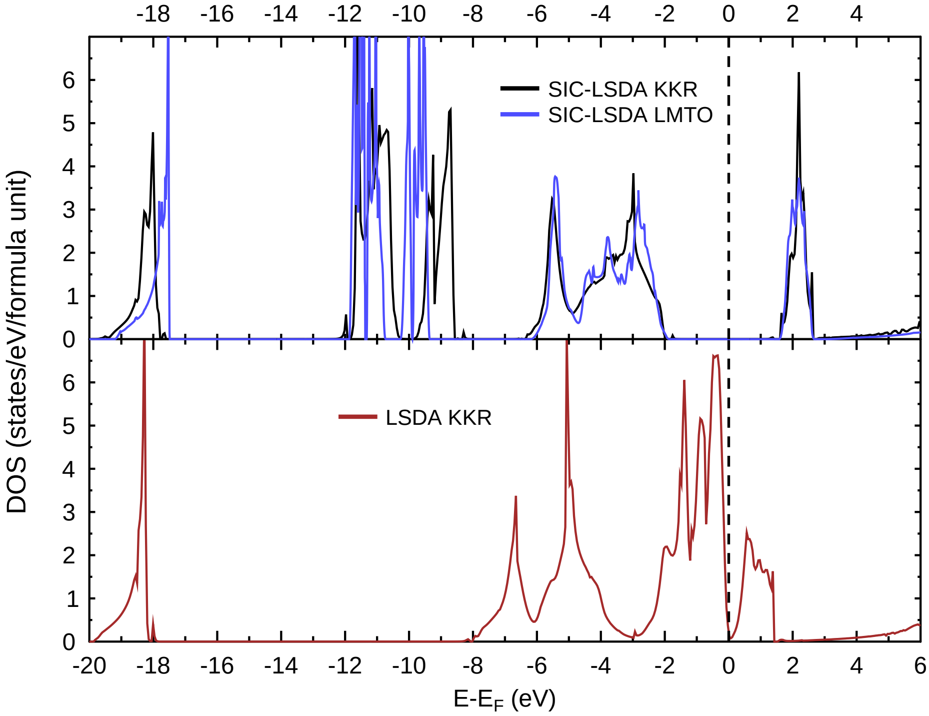

Figure 1: Density of states of NiO calculated with the SIC-LSDA-LMTO (blue line) and LSIC-LSDA KKR (black line) implementations for the low temperature anti-ferromagnetic state. The SIC results of two different implementations are very similar [39].

Other properties of TMO's are compared in Table 1. The results show a significant improvement of the SIC-LSDA calculations of the equilibrium lattice constant, local magnetic moment, and the band gap in comparison to the LSDA approach. For all TMO's the equilibrium lattice constants, obtained within the LSDA, are too small, while our LSIC-LSDA calculations overestimate them slightly, but show the correct trend for the whole series. The same trend can be seen for local magnetic moments on the transition metals, which are getting larger in comparison to the LSDA results and are in good agreement with the experimental values except for CoO (this is due to missing the spin orbit coupling which should increase the moment). Our local moments are also comparable to the results obtained with the full SIC-LSDA LMTO implementations. The LSIC-LSDA approach increases systematically the size of the band gaps for all TMO's. However, the band gap is an excited state property and can not be correctly described with the SIC-LSDA method, since the latter is designed for the description of the ground state. Nevertheless, unlike in other local DFT approximations, in the SIC-LSDA formalism there is a contribution to the magnitude of the band gap from the discontinuity of the exchange-correlation potential, in particular when the states defining the gap are SI corrected.

Table 1: Lattice constants, local magnetic moments and the band gaps for the series of transition metal oxides of our implementation, two other implementations and the corresponding experimental values. The values in round brackets for the magnetic moment are calculated at the experimental lattice constant.

	Compound				
	MnO	FeO	CoO	NiO	CuO
lattice constant [Å]					
LSDA KKR	4.27	4.13	4.05	4.01	4.08
SIC-LSDA KKR	4.49	4.39	4.31	4.24	4.27
Expt.	4.446 [41],4.44 [42]	4.326 [43]	4.26 [42,44]	4.176 [45],4.17 [42]	4.245 [44]
local magnetic moment on TM [μ_B]					
LSDA KKR	4.11(4.27)	3.26(3.40)	2.20(2.33)	0.85(0.97)	0.00(0.00)
SIC-LSDA KKR	4.63(4.60)	3.68(3.66)	2.69(2.68)	1.68(1.67)	0.76(0.76)
Expt.	4.79*,4.58*	3.32*	3.35* [46], 3.8*	1.77*,1.64*,1.90*	0.65*
SIC-LSDA LMTO [31]	4.49	3.54	2.53	1.53	0.65
SIC-LSDA LMTO [32]	4.64	3.55	2.59	1.49	0.64
bandgap [eV]					
LSDA KKR	0.83 (0.73)	0.00 (0.00)	0.00 (0.00)	0.23 (0.23)	0.00 (0.00)
SIC-LSDA KKR	3.07 (3.25)	3.38 (3.54)	2.78 (2.81)	3.56 (3.76)	1.52 (1.57)
Expt.	3.6-3.8*	2.4 [47],2.5 [48]	2.4*	4.3*,4.0*,4.3 [49]	1.37*
SIC-LSDA LMTO [31]	3.98	3.07	2.81	2.54	1.43
SIC-LSDA LMTO [32]	3.57	3.25	2.51	2.66	1.00

* taken from ref. [31], for detailed references see references therein.

3.2 Exchange interaction and transition temperature

Here we discuss magnetic exchange interactions of MnO, FeO, CoO, and NiO. The exchange constants J_{pr}, which enter the Heisenberg Hamiltonian (9), can be directly estimated from Eq. (10) using the Green function method [26]. In our study [40], the Green function was calculated for the ground state (the AFII structure with the equilibrium lattice constants from Table 1). The corresponding exchange constants J_{ij} were obtained for the first 11 neighbour shells. As expected, only the first two of them, J_1 and J_2 are of relevance, which agrees well with the idea of the super-exchange mechanism. The J_{pr} can be as well extracted from the total energy differences for a number of magnetic structures and mapping them onto the Heisenberg Hamiltonian. In this approach the total energies of the TMO's in the ferromagnetic (FM) and antiferromagnetic AFI and AFII configurations are taken into account. The AFI structure is characterized by oppositely magnetized planes which are stacked along the (001)-direction, while in the AFII the planes are stacked along the (111)-direction. The mapping onto the Heisenberg Hamiltonians yields

$$J_1 = \frac{1}{16}\left(E_{AFI} - E_{FM}\right) \tag{12}$$

and

$$J_2 = \frac{1}{48}\left(4E_{AFII} - 3E_{AFI} - E_{FM}\right) , \tag{13}$$

where J_1 describes the interaction between the nearest neighbours and J_2 that of the next nearest neighbours. The choice of the three above mentioned structures restricts the method to the determination of J_1 and J_2 only. Using more magnetic structures and hence calculating more exchange parameters is in principle possible. However, due to the nature of the present exchange mechanism, the super-exchange, this has usually not been done.

The J_{ij}, obtained with these two approaches, are shown in Table 2, in which we compare the calculated exchange constants with the experimental results. From Table 2 one finds that the J_2 parameters constitute the major part of magnetic exchange in TMO's and that in magnitude they agree reasonably well between the two theoretical approaches, the magnetic force theorem (MFT) and ΔE, energy difference, methods. The results are about 70-80% of the experimental values, except for FeO, where the agreement for the MFT J_2 is almost perfect and the ΔE is larger than the experimental one. This rather accidental agreement can be attributed to the fact that the experimental values were measured for Wüstite samples $\mathrm{Fe}_{1-x}\mathrm{O}$ with $x \neq 0$ [50]. However, both theoretical approaches provide the experimental trend of an increase of the absolute value of J_2 across the TMO series, which can be associated with the increasing number of $3d$ electrons, responsible for the magnetic exchange.

The situation is very different for the J_1 exchange parameters. From our results in Table 2 one can see that, with the exception of NiO, the absolute magnitudes of J_1 are, within about 30%, similar for the two theoretical approaches, but the sings are opposite. The results of the MFT calculations show the opposite trend to that found for J_2: the antiferromagnetic coupling is getting weaker as one moves from MnO to CoO, and in NiO it becomes ferromagnetic. The reason for this is a competition between a direct and an indirect exchange between the nearest neighbour TM atoms. In the case of MnO, the Mn atom has half-filled d shells that leads to antiferromagnetic coupling since an electron hopping from one Mn to the other one keeps its spin. Moving across the TMO series the occupation of the minority spin channel is growing. This increases the probability of an electron hopping, if the nearest neighbour TM atoms are ferromagnetically aligned. The indirect exchange between nearest neighbour TM atoms can be explained within Goodenough model [51]: nearest TM neighbours interact antiferromagnetically when two electrons in the same oxygen p or s orbital are excited to the empty TM e_g orbitals. The strength of this interaction does not change much across the TMO series since the occupation of both the oxygen p or s and the TM e_g orbitals is almost constant. On the other hand, the ferromagnetic coupling is provided by electrons of alike spin that are in different orbitals of the oxygen atom. Its strength grows with the occupation of t_{2g} orbitals, which is rising across the TMO series from MnO to NiO. Thus, the antiferromagnetic coupling does not change much, while the ferromagnetic interaction increases with the occupation of the $3d$ shells of TM atoms, which can be clearly seen in the MFT values for J_1 in Table 2.

Next, we discuss the transition temperatures of TMOs. The transition temperature can be calculated from different approximations. In our work we used the mean-field approach (MFA), the random phase approximation (RPA) [52] and Monte Carlo (MC) simulations. In addition, we estimated the Néel temperatures of TMOs using the DLM method [19, 20]. The calculated transition temperatures are presented in Table 3. One finds that the MFA overestimates the experimental Néel temperatures, whereas RPA underestimates them, which is expected from the general consideration [53]. One can also see that the Néel temperatures calculated with J_1 and J_2 only do not differ significantly from those calculated using 11 neighbour shells, supporting the idea of superexchange. The RPA and MC results for MnO and FeO are relatively small in comparison to experiment. This can be explained by an underestimation of exchange constants since the SIC-LSDA can slightly overestimate spatial localization of $3d$ orbitals. The DLM results are, with the exception of NiO, in good agreement with experimental values. The trend of the DLM calculations is opposite to the RPA and MC results, namely the ratio $\mathrm{T}_N^{DLM}/\mathrm{T}_N^{exp}$

becomes smaller with increasing atomic numbers. This could be due to not taking into account the quantum character of the system, which in the present calculations have been approximated by the factor $(S+1)/S$, where S is determined according to Hund's rules.

Table 2: The exchange parameters, J_i, in meV, with i being the shell index, for the first two shells of all the studied TMOs and both the magnetic force theorem (MFT) and ΔE, energy difference, methods. The experimental (exp.) values are given in the leftmost column, respectively, according to the Hamiltonian in Eq. (9). For $i > 2$, the absolute magnitudes of the J_i's for all the TMOs have been less than 0.1 meV. For both the MFT and ΔE approaches the calculated equilibrium lattice constants from Table 1 have been used.

TMO	J_1			J_2		
	exp.	MFT	ΔE	exp.	MFT	ΔE
MnO	-2.06, -2.64 [54]	-0.91	0.68	-2.79 [54]	-1.99	-1.65
FeO	1.04, 1.84 [50]	-0.65	0.48	-3.24 [50]	-3.17	-3.50
CoO	0.70 [55], -1.07 [56]	-0.32	0.53	-6.30 [55], -5.31 [56]	-4.84	-4.40
NiO	-0.69 [57], 0.69 [58]	0.15	1.42	-8.66 [57], -9.51 [58]	-6.92	-6.95

Table 3: Summary of the Néel temperatures calculated with the J_{ij} from the MFT approach (see Table 2). In the top two rows the experimental and the DLM values are listed, followed by the RPA values based on the interaction of the first 11 TM-TM-shells and of only the nearest and next-nearest neighbours (i.e. only J_1 and J_2). In rows 5 and 6 the MFA results shown, again using 11 or 2 shells, respectively. In the last row the results of the Monte Carlo simulations are presented.

T_N [K]	MnO	FeO	CoO	NiO
Experiment	118	192	289	523
DLM [38]	126	172	242	336
RPA with J_{1-11}	81	146	252	440
RPA with $J_{1,2}$	87	155	260	448
MFA with J_{1-11}	122	210	362	628
MFA with $J_{1,2}$	129	221	373	644
MC	90	162	260	458

3.3 Magnon spectra

Based on the obtained exchange constants, we calculated the magnon spectra of all studied TMO's, shown in Fig. 2 together with the experimental results. Generally, the agreement between the calculated magnon dispersion curves and the experimental observations is good. On the whole, the theoretical curves underestimate the experimental energies, except for FeO, which is due to the underestimation of the J_2 parameters. The relative magnitude of the peak along $[qqq]$ varies strongly, as one goes through the TMO's series, This effect can be ascribed to the changing ratio of J_2/J_1. The results, presented above, were obtained at T=0 K. In a ferromagnet at T=0 K the electronic band structure is spin-polarized. With increasing temperature, spin fluctuations are induced, which eventually destroy the long-range magnetic order and hence the overall spin polarization. These collective electron modes interact as the temperature increases, depending upon and affecting the underlying electronic structure. For many materials, including magnetic semiconductors, the magnetic excitations can be modelled by associating local spin-polarization axes, $\{\hat{e}\}$, with all lattice sites which vary very slowly on the timescale of the electronic motions.

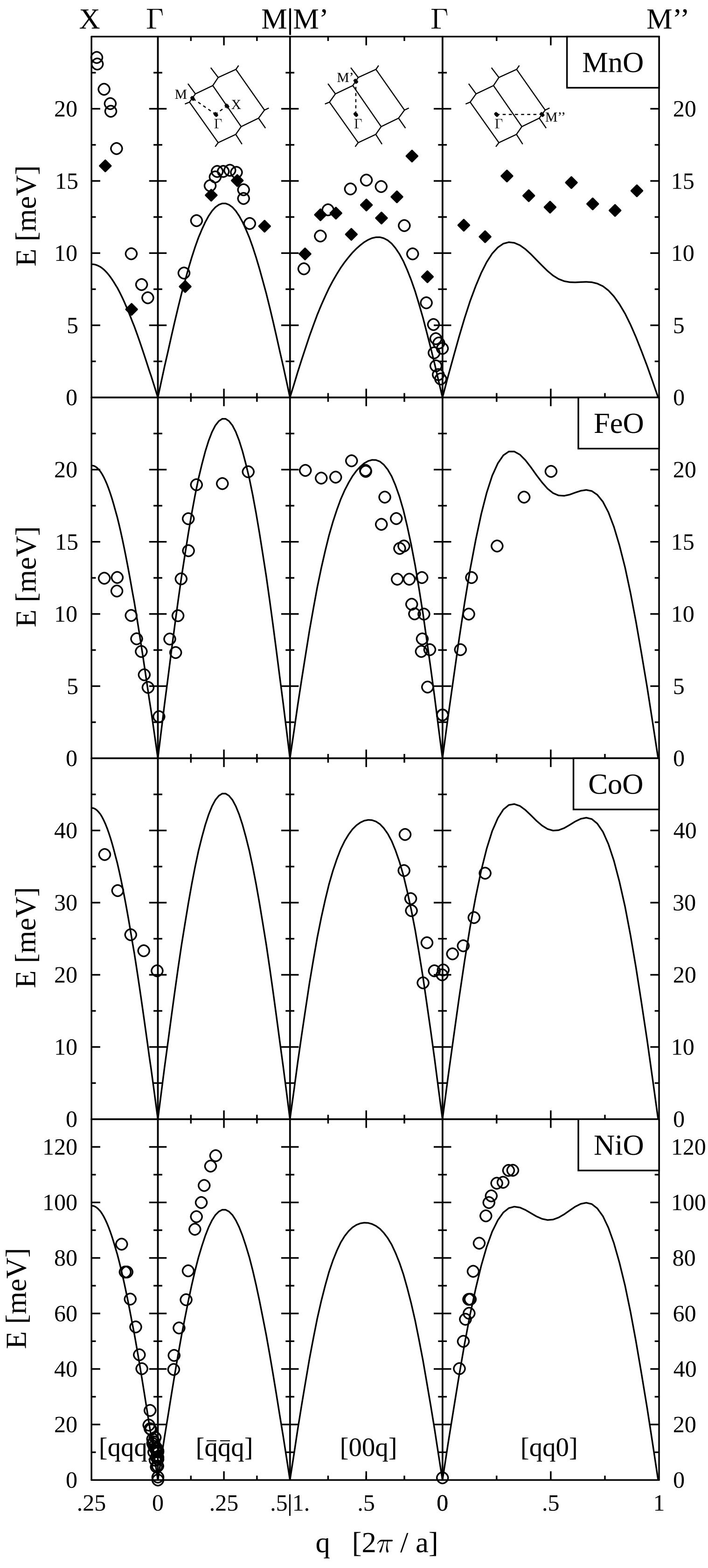

Figure 2: Shown are the calculated TMO spin wave dispersions together with experimental data points for MnO (black diamonds [59], open circles [54]), FeO [50], CoO [55] and NiO [58], respectively. The coordinates are Cartesian and in units of $2\pi/a$. The path chosen along several high symmetry lines starts at X= $(0.25, 0.25, 0.25)$ and goes along $[qqq]$ to $\Gamma = (0, 0, 0)$, then along $[\overline{q}\overline{q}q]$ to M= $(-0.5, -0.5, 0.5)$, and further along $[00q]$ to Γ of the neighbouring AFII Brillouin zone, then continuing along $[qq0]$ to M''. The inlays in the MnO panel show the different branches along the AFII Brillouin zone.

These local moment degrees of freedom produce local magnetic fields on the lattice sites which affect the electronic motions and are self-consistently maintained by them. By taking appropriate ensemble averages over the orientational configurations, the system's magnetic properties can be determined. In particular, consideration of spin fluctuations above the transition temperature (paramagnetic state) can provide information about the type of ordering that is likely to occur as the temperature is lowered through a phase transition. This can be done within the DLM formalism as it is implemented within the multiple scattering theory [19, 20]. The disordered local moment method sets up a mean field treatment without the intermediate step of fitting to an effective Heisenberg model. It uses the CPA to average over the local moment configurations. By considering the response of the paramagnetic state, where the local moments have the same probability of being oriented in any direction, to an external magnetic field the onset of magnetic order and magnetic transition temperature can be determined. The resulting susceptibility has the form $\chi(\mathbf{q}) = \mu^2/(3k_BT - S^2(\mathbf{q}))$, where $S^2(\mathbf{q})$ is the direct spin correlation function.

In Ref. [38], we applied the DLM method to study paramagnetic spin fluctuations of TMO's. In particular, we investigated wavevector dependence of the susceptibility $\chi(\mathbf{q})$ taking into account the electronic correlations within the SIC-LSDA method. In Fig. 3, we present the results of our paramagnetic susceptibility calculations for MnO. These show the paramagnetic state to be dominated by spin fluctuations with wavevector $\mathbf{q}_{max}$=(0.5,0.5,0.5) (in units of 2π/lattice constant). This indicates that the system will order into an antiferromagnetic type II structure, where moments within a $\langle 111 \rangle$ layer are aligned but are antiparallel in successive layers. This concurs with the experimentally observed ground state of this system and also T=0 K calculations [39], where the most stable structure was determined by comparing the total energies of different magnetic configurations.

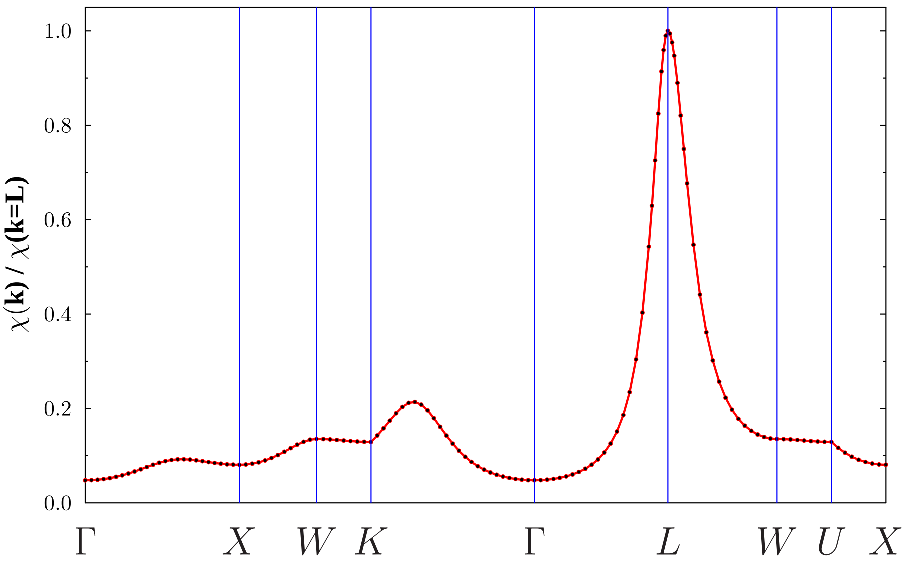

Figure 3: Paramagnetic susceptibility of MnO, as a function of wave vector **k**.

We examine the temperature dependence of the static spin susceptibility $\chi(\mathbf{q})$, in particular

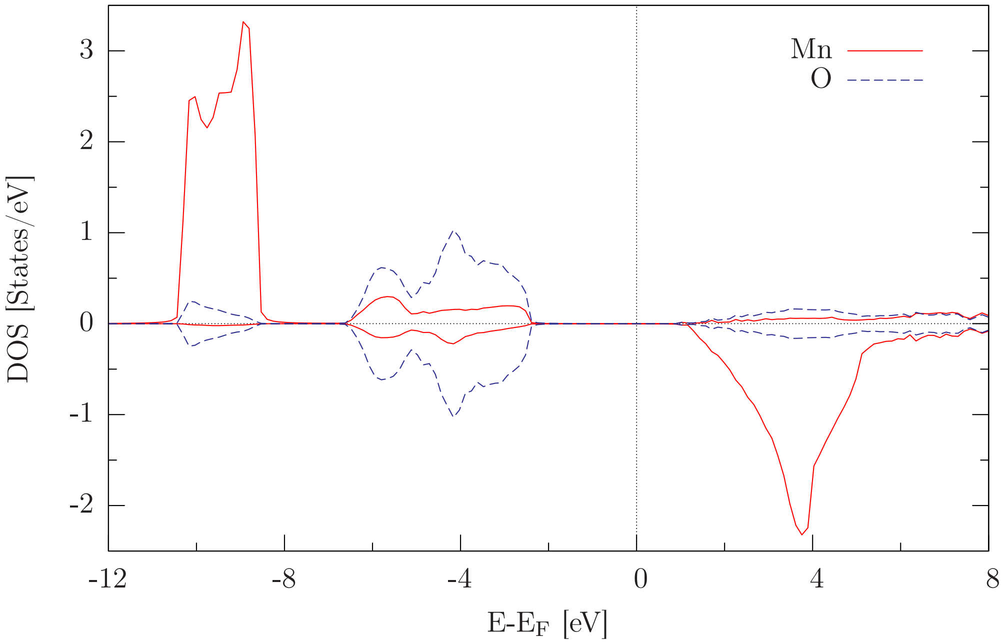

Figure 4: The local density of states (DOS) for MnO in its paramagnetic (DLM) state on Mn (full line) and O sites (dashed). The upper (lower) panel shows the DOS associated with electrons with spins parallel (anti-parallel) to the local moment on the site. Note that a sizeable gap persists in the paramagnetic state.

looking for a divergence which would signify that paramagnetic state becomes unstable with respect to the formation of a spin density wave, characterized by the wavevector $\mathbf{q}_{max}$. For the theoretical (experimental) lattice parameters, such a divergence occurs at 102 K (103 K). This mean field estimate of the Néel temperature is in good agreement with the experimental value of 118 K. The Néel temperatures of other TMO's are presented in Table 3 and were already discussed above.

Finally, it is perhaps useful to add here, that combining DLM with LSIC leads also to a well defined band gap in the paramagnetic state of TMO's, whose magnitude is very much the same as in their AFII ground states. [38] This shows that in SIC-LSD band gaps can be obtained without imposed magnetic order and that at high temperatures our DLM-LSIC approach competes well with the LDA+DMFT approach. To demonstrate this in Figure 4 we show the local DOS for the paramagnetic DLM state of MnO, where an exchange-splitting is evident. Of course, when an average is taken over all local moment orientations, the electronic structure does not have an overall spin-polarisation. Nevertheless, it is possible to identify such 'local exchange splitting' experimentally, using photoemission and inverse photoemission techniques. The local moment obtained for the Mn sites in the DLM paramagnetic state differs from that in the groundstate by $\approx 0.03\mu_{\mathrm{B}}$ (see the table above). Such a small change between the ordered (zero temperature) and disordered (high temperature) states justifies our DLM picture, where the magnitude of the 'local exchange splitting' is independent of the orientational configurations of the moments. Furthermore this feature is the cause of the spin-summed electronic structure showing little difference between the paramagnetic state above T_N and the magnetically ordered ground state. Notably a sizeable band gap at the Fermi energy persists into the paramagnetic phase as found experimentally.

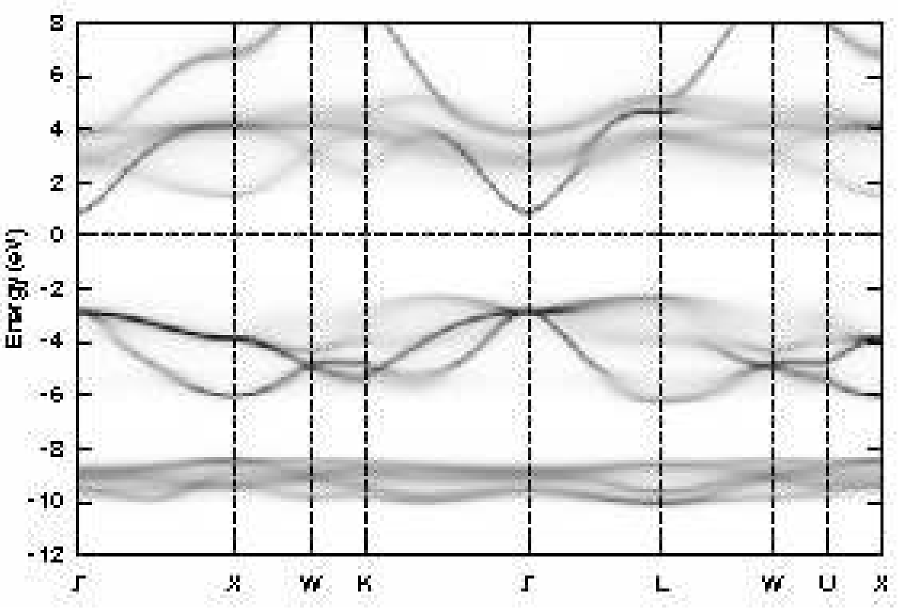

Figure 5: The electronic structure for MnO in its paramagnetic (DLM) state along symmetry directions. The loci of the peaks of the Bloch spectral function are displayed and the shading shows the broadening of these quasi-particle peaks caused by the spin fluctuation disorder.

Figure 5 shows the electronic structure of the paramagnetic (DLM) state in more detail and demonstrates the wave-vector, $\mathbf{k}$, dependence of the local exchange splitting. This figure is constructed from calculations of the Bloch spectral function, $A_B(\mathbf{k}, E)$. For non-interacting electrons in an ordered system at $T = 0$K, $A_B(\mathbf{k}, E)$ comprises a set of Dirac delta functions which trace out the electronic band structure. When electron interaction, finite temperature or disorder effects are included the spectral function is a set of broadened peaks describing quasi-particle excitations. The broadening of the peaks shown in Figure 5 is a consequence of the local moment disorder in the paramagnetic state [38].

4 Diluted magnetic oxides

Diluted magnetic oxides (DMO's) are promising materials for a new class of devices, based on the use of both charge and spin degrees of freedom. DMO's are wide band gap insulating semiconductors, which are usually doped with transition metals. The physical mechanisms underlying ferromagnetic order in these systems are still elusive, although in the meantime some consensus has been reached that ferromagnetic ordering might be intrinsic in nature and not simply related to the precipitation of metallic clusters. The presence of magnetic ions can influence the free carrier behavior through the $sp - d$ exchange interaction between the localized magnetic moments and the spin of the itinerant carriers [60]. Parallel to spectroscopic evidence that transition metals are substituting cations of the oxide, several mechanisms for the stabilization of ferromagnetism were discussed, involving an indirect carrier-mediated exchange mechanism [60], the percolation of polarons [61, 62], or the presence of uncompensated spins at the surface of nanocrystals [63]. Using SIC-LSD approximation we have investigated the ground state valency configuration of transition metal (TM=Mn, Co) impurities in $p-$ and $n-$type ZnO. [64, 65] We have found a stable localized TM^{2+} configuration for a TM impurity in ZnO, if no additional hole donors have been present. This configuration has been energetically favoured over the itinerant $d-$electron configuration of the local spin density picture. Our calculations indicate furthermore that the $(+/0)$ donor level is situated in the band gap, in agreement with experiments, [66, 67] as a consequence of which the TM^{3+} becomes more favourable in $p-$type ZnO, where the Fermi level E_F is positioned near the top of the valence band. In this scenario, modelled here by co-doping with N, the additional delocalized $d-$electron charge transfers into the entire states at the top of the valence band, and hole carriers will only exist, if the N concentration, $[N]$, exceeds the TM impurity concentration, $[TM]$. This implies, that the applicability of the Zener model, as proposed by Dietl *et al.*, [68] can only be valid in the case when $[N] > [TM]$. Since, however, co-doping with N has revealed itself to be a difficult task, [69] fulfilling the latter criterion constitutes a considerable hurdle with regard to actually synthetising these DMS. For the $n-$type conditions, with the Fermi energy E_F close to the conduction band minimum, TM impurity remains in the 2+ charge state.

There has been extensive search to find DMO's that are ferromagnetic at room temperature. Much attention was devoted to materials based on ZnO, which was identified as one of the promising candidates for transparent electronic applications owing to its exciting optoelectronic properties. Several groups have reported the observation of room temperature ferromagnetism in TM-doped ZnO based systems. Unfortunately, many of these results are not or hardly reproducible, which demonstrates an incomplete understanding of the underlying mechanism of magnetism of these systems.

One of the main difficulties of theoretical considerations of DMO's is a lack of information about the crystal structure and their chemical composition. Usually DMO's are fabricated using epitaxial-growth technologies under far from equilibrium conditions. Therefore, an exact determination of their crystal structure is often not possible either with experiments or first-principles methods. One way to get more insight is a comparison of particular properties of DMO's, found by first principles simulations, with experiment. First-principles method can often provide an adequate description of many observable phenomena. The crystal structure can be used as a parameter in such simulations. Varying atomic positions and the chemical composition, one can achieve an acceptable fit of a particular observable quantity. The structural information, obtained in this way, can be used for investigations of other properties of the considered system. One of the observable quantities, which can be adequately calculated for many systems from first-principles, is the x-ray absorption spectrum (XAS) as well as x-ray magnetic circular dichroism (XMCD), which is the difference of the x-ray absorption spectra with opposite (left and right) directions of circular polarization.

4.1 A study of (Zn,V)O

As an example of such complementary investigations, we demonstrate here a study of structural, electronic and magnetic properties of (Zn,V)O diluted magnetic oxide. This system was studied by several experimental groups using x-ray absorption (XAS) and x-ray magnetic circular dichroism (XMCD) experiments. The XAS was measured at the V K edge [70] and field and temperature dependences of the XAS and XMCD spectra at the V $L_{2,3}$ edges in the $(Zn_{1-x}V_x)O$

(x=0.05) were reported by Ishida *et al.* [71]. They found a linear increase of the XMCD signal with external magnetic field H which indicates that the paramagnetic signal dominates the XMCD signal and that the ferromagnetic component is small, consistent with their magnetization measurements. The majority of the V ions were presumably strongly coupled antiferromagnetically. They estimated that ∼10% of the V ions were paramagnetic, ∼90% were presumably strongly coupled antiferromagnetically, and the ferromagnetic component was below the detection limit of XMCD. In our study we simulate the XAS and XMCD spectra from first-principles using the crystal structure, the chemical composition and the magnetic order as external parameters. The obtained information is used for the extensive study of electronic and magnetic properties of (Zn,V)O DMO's.

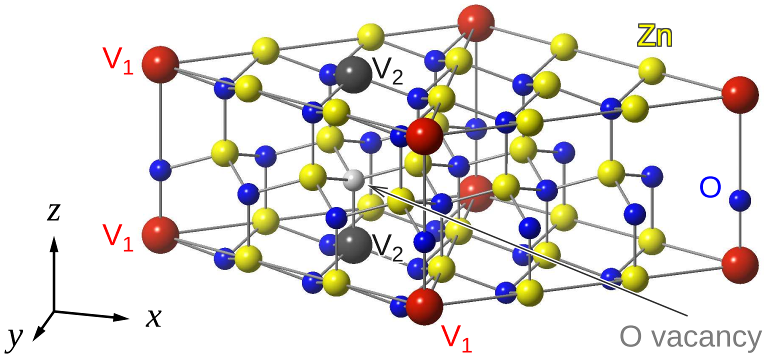

Figure 6: Schematic representation of the (Zn,V)O structure with two substituted V atoms with the largest possible V–V for a giving concentration interatomic distance (see the text).

In Fig. 6 we show the supercell of the wurtzite-type ZnO unit cell with one or two of the Zn ions replaced by V. Previous experimental and theoretical studies suggest that there is no clear site preference for the V atoms in bulk ZnO and V doping in ZnO is almost homogeneous. The substitutional ($Zn_{1-x}V_x$)O positions are illustrated in Fig. 6 for a 36-atom ZnO unit cell containing two substitutional V atoms (x=0.1111) for the largest possible V–V interatomic distance of [5.53]Å. The crystal structure was optimized using the Vienna *ab initio* simulation package (VASP). [36] The crystal structure obtained with the VASP code served as input in the calculations of x-ray absorption and dichroism spectra within an fully relativistic LMTO implementation [34].

Since the real structure and chemical composition of ($Zn_{1-x}V_x$)O was not known, we performed numerous calculations fitting XAS and XMCD spectra to the experimental results. The fitting parameters were positions of V atoms, Zn excess atoms, various oxygen vacancies and the magnetic order of V atoms. The best fit is shown in Fig. 7, which presents the calculated XAS as well as XMCD spectra of the ($Zn_{1-x}V_x$)O DMS (for x=0.1111) at the V $L_{2,3}$ edges compared with the experimental data. [71] In this model, V atoms substitute cations and are antiferromagnetic to each other. Thereby, they are positioned at the largest possible V_1–V_2 distance of [5.53]Å (see Fig. 6). A relevant XMCD signal is possible only in the presence of oxygen vacancy located in the first neighbourhood of the second V_2 atom along z direction (see Fig. 6). Adding Zn excess atoms also improves the agreement between the theory and the experiment.

The X-ray absorption spectrum at the V L_3 edge is rather complicated and consists of two major peaks c and d at the [515.6]eV and [517]eV, respectively, with two low energy additional shoulders a and b at the [513.8]eV and [514.6]eV and a high energy shoulder at the [518]eV. As can be seen from the top panel of Fig. 7 the calculations for an ideal crystal structure with two substituted AFM ordered V_1 atoms (full green curve) provide a correct description of the x-ray absorption intensity only for the peak c and shoulder b. The full explanation of the spectra is possible only if crystal imperfections are taken into account.

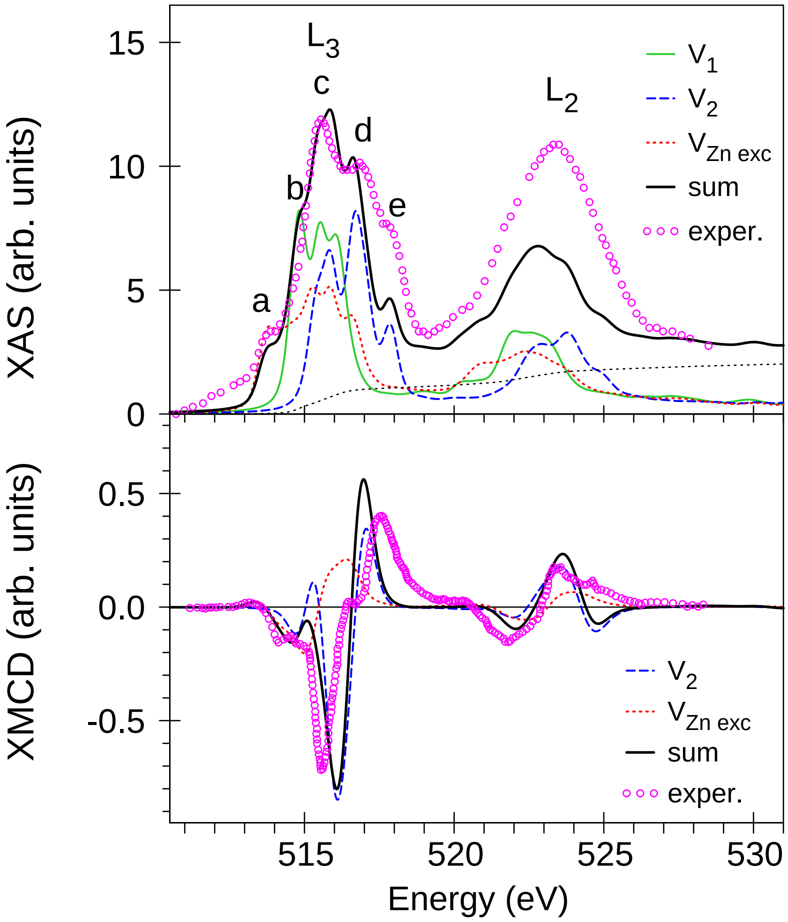

Figure 7: (Color online) Top panel: theoretically calculated (thick full black line) and experimentally measured [71] (circles) x-ray absorption spectra of $(Zn_{1-x}V_x)O$ at the V $L_{2,3}$ edges. Full green line presents the x-ray absorption spectrum without any additional defects. Dashed blue and dotted red lines present the XA spectra with the oxygen vacancy and Zn exceed atom, respectively. Bottom panel: theoretically calculated (thick full black line) and experimentally measured [71] (circles) XMCD spectra at the V $L_{2,3}$ edges. Dashed blue and dotted red lines present the XMCD spectra with the oxygen vacancy and Zn exceed atom, respectively.

For a better understanding of electronic and magnetic properties the electronic structure of $(Zn_{1-x}V_x)O$ was studied in three different configurations: (i) the ideal wurtzite structure with ferromagnetically ordered V, and the model, elucidated from the XAS and XMCD experiments, with antiferromagnetically ordered V in presence of an oxygen vacancy in (ii) ideal and (iii) relaxed geometries.

Figure 8 presents total and partial density of states for a 36-atom ZnO wurtzite unit cell containing one V substitution (x=0.06) in the LSDA (model (i)). The O s states are located mostly between [-21.0] to [-19.7]eV below the Fermi level and the p states of the O are found between [-9.6]eV to [-3.0]eV. The spin splitting of the O p states is quite small. Zn d states occupy the energy interval between [-9.6] and [-3.0]eV and hybridize strongly with the O p states.

The magnetic moment in the (Zn,V)O unit cell is [2.088]μ_B. Our band structure calculations yield a spin magnetic moment of [1.920]μ_B for the V atoms in $(\mathrm{Zn}_{1-x}\mathrm{V}_x)\mathrm{O}$ (x=0.06). The induced spin magnetic moments at the O first neighbour sites are [0.004]μ_B, and [-0.003]μ_B, for longer and shorter distant O atoms, respectively. Twelve Zn ions in the second neighbour shell couple ferromagnetically to the substituted V ion with spin magnetic moments from [0.034]μ_B, to [0.068]μ_B. The orbital moments at the Zn and O sites are small with the largest one at the O first neighbour sites ([0.001]μ_B). The orbital magnetic moment at the V site is [-0.082]μ_B and is antiparallel to the spin moment.

Figure 9 presents vanadium d and oxygen p partial density of states for $(\mathrm{Zn}_{1-x}\mathrm{V}_x)\mathrm{O}$ wurtzite unit cell containing two V substituted atoms (x=0.1111) ordered antiferromagnetically and one oxygen vacancy near the V_2 atom (see Fig. 6), at close vicinity of the Fermi level. The oxygen vacancy has four nearest neighbours atoms: three Zn atoms at a distance of [1.9496]Å and one V atom at [1.9505]Å. The vacancy does not affect much the energy distribution of the partial DOS's without taking into account the lattice relaxation (model (ii), full blue lines in Fig. 9). However, it strongly affects the shape and energy position of the partial DOS's for the relaxed lattice (model (iii), dashed red curves) placing V_2 d states right to the Fermi level and V_1 d states in its close vicinity. The lattice relaxation causes a shift of the V_2 atom and three Zn atoms the towards vacant place by the [0.14]Å and [0.26]Å, respectively.

The structural model, elucidated from our XAS and XMCD simulations, was utilized for calculations of the corresponding electronic structure and exchange parameters using the KKR Green function method in the multiple scattering representation. [72] The schematic representation of the exchange interaction between the magnetic moments of the nearest neighbours is shown in Fig. 10.

The strongest magnetic interactions were found between V atoms only if there is either an oxygen atom or an oxygen vacancy in between (see Fig. 6 and Fig. 10(a,b) respectively). Thereby, one can distinguish two different vanadium atoms: V_1 far from and V_2 close to an oxygen vacancy. The exchange interaction between V_1 and V_2 atoms is very small since the atoms are separated by [5.53]Å and there is no connecting atom in between (see Fig. 6 and Fig. 10(c)). The exchange interaction in V_1–V_1 is mediated mainly by the oxygen between the vanadium atoms and is positive leading to a ferromagnetic order for this pair (see J_{01}^{11} at zero relaxation in Fig. 11(b)). This changes if the oxygen is replaced by a vacancy (V_2–V_2 pair) in accordance with our structural model. Removing the oxygen atom kills the exchange interaction between the neighbouring vanadium moments (see J_{01}^{22} at zero relaxation in Fig. 11(b)). However, the atoms around the vacancy experience strong relaxations and this promotes an antiferromagnetic order for this pair. Our simulations show that the exchange interaction is very sensitive to these atomic movements. We found that most substantial changes of J_{ij} occur when the neighbouring Zn atoms move towards the vacancy (see inset in Fig 11), while relaxations of V and O atoms are insignificant for the magnetic interaction. According to our structural optimizations the shift of the Zn atoms is about [0.26]Å. Due to these relaxations, the exchange parameters between the first neighbours J_{01}^{22} were changed from $\approx$[0]meV in the non-relaxed geometry to -16 meV. The interaction between the second neighbours experiences also significant changes and

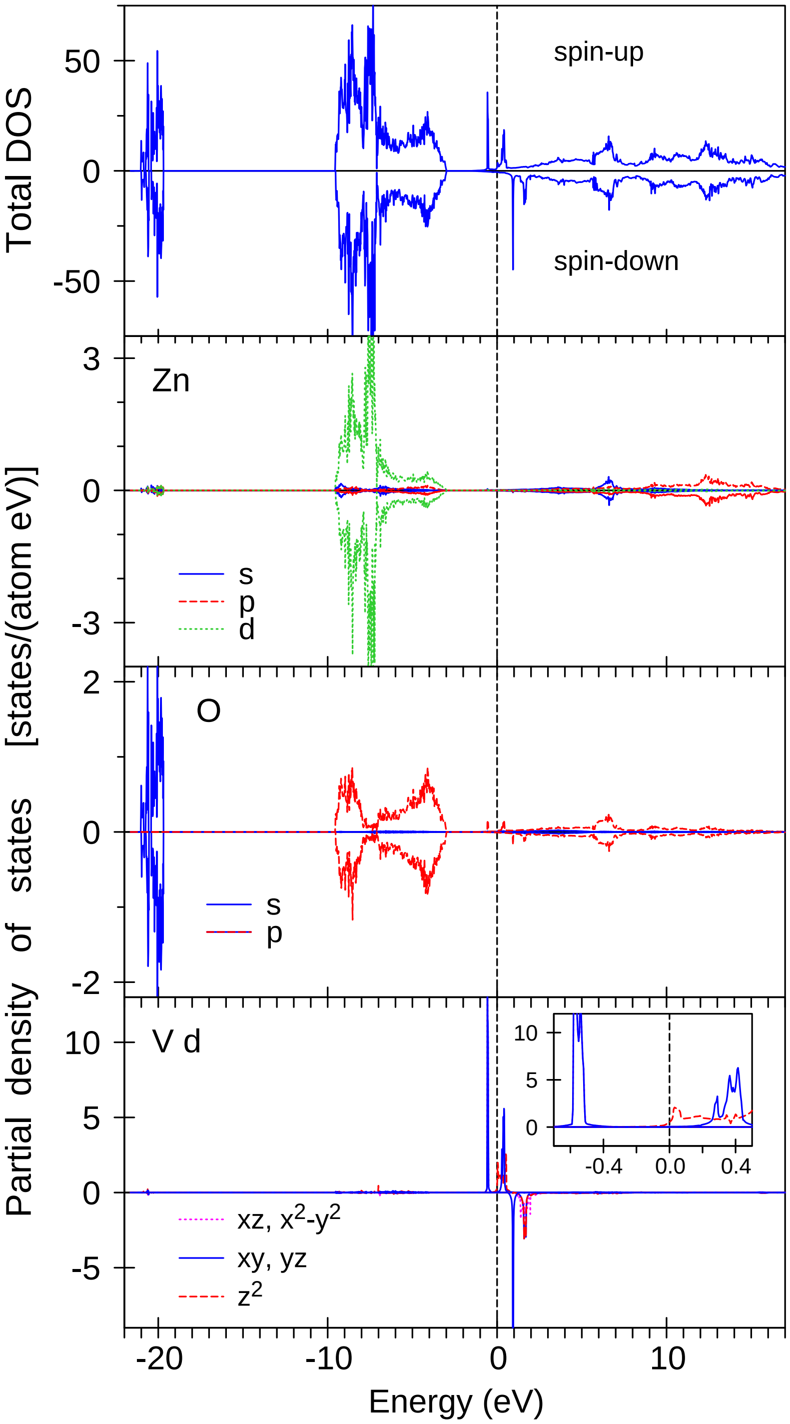

Figure 8: The LSDA total [in states/(cell eV)] and partial [in states/(atom eV)] densities of states, calculated by the LMTO method, for the O, Zn and substituted V ions in $(Zn_{1-x}V_x)O$ (x=0.06, model (i), see text for details). The insert is a blowup of the V d PDOS close to the Fermi energy. The Fermi energy is at zero.

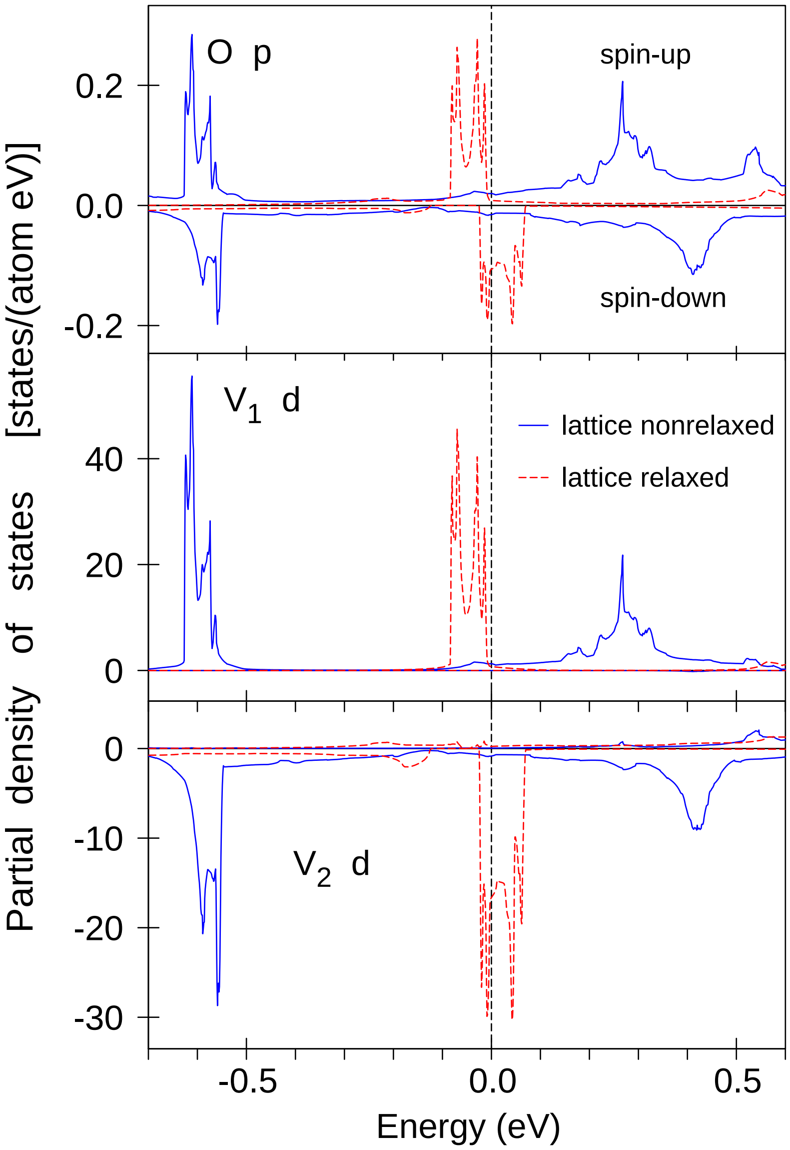

Figure 9: The LSDA d-partial [in states/(atom eV)] densities of states, calculated by the LMTO method, for the substituted V_1 and V_2 ions in $(Zn_{1-x}V_x)O$ middle and lower panels, respectively (see the explanation in the text). Upper panel presents O p partial density of states. Full blue and dashed red lines show the results for non-relaxed (model (ii)) and relaxed (model (iii)) lattices. The Fermi energy is at zero.

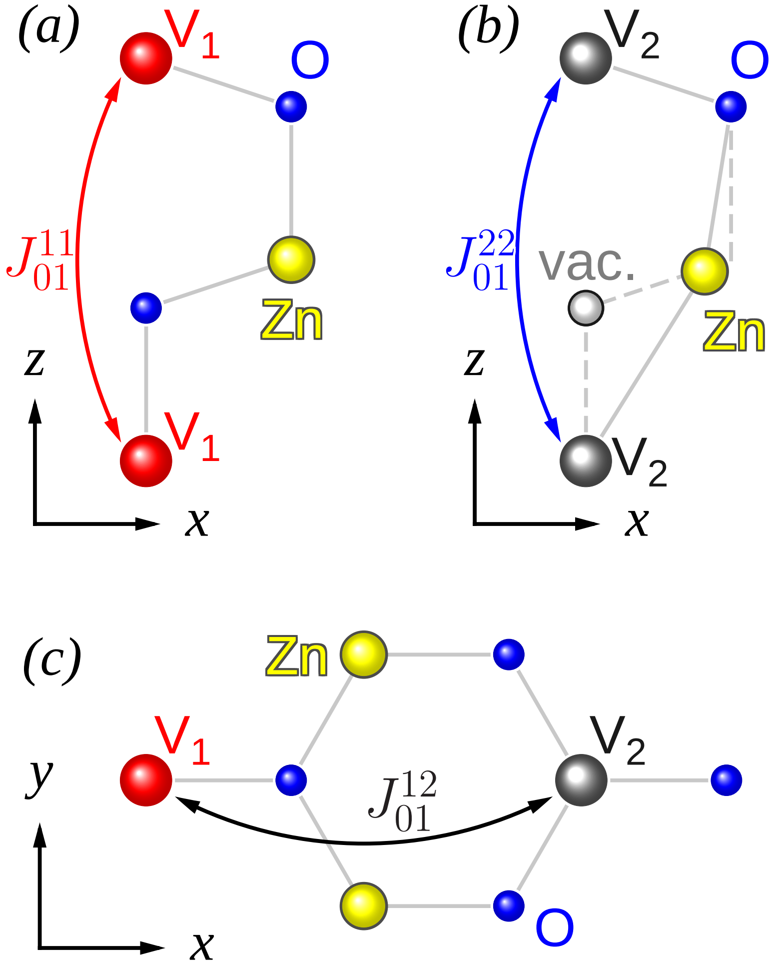

Figure 10: Schematic representation of magnetic interactions between V atoms in $(\mathrm{Zn}_{1-x}\mathrm{V}_x)\mathrm{O}$: (a) two V atoms substituting Zn positions with an oxygen in between. (b) two V atoms within an oxygen vacancy in between; (c) V_1–V_2 pair (see the text for explanation). The dashed line in (b) shows ideal wurtzite structure.

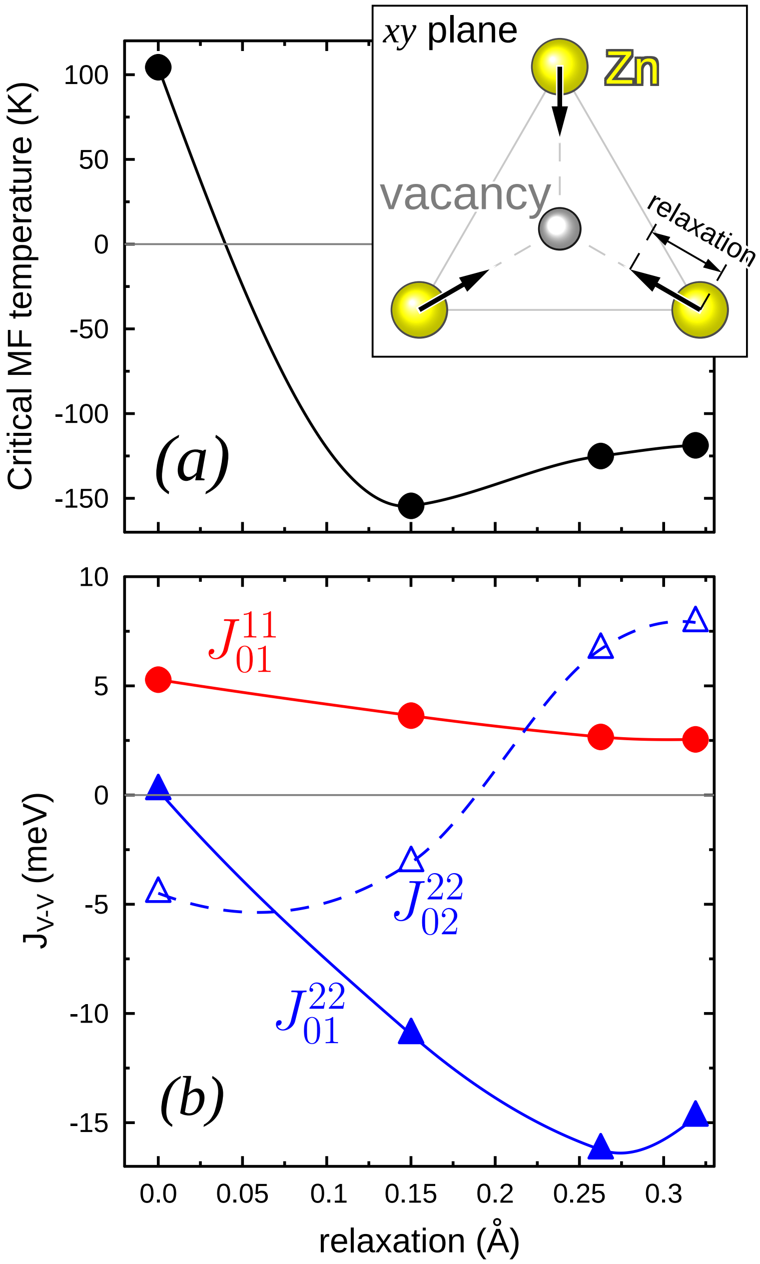

Figure 11: Critical temperatures (a) and exchange parameters (b) for $(Zn_{1-x}V_x)O$ calculated for various positions of atoms around an oxygen vacancy. Inset shows scheme of movements of Zn atoms towards to the vacancy.

is positive at the relaxed geometry. This suggests that the V_2–V_2 pair with an oxygen vacancy is antiferromagnetic. The vanadium pairs V_1–V_1 without oxygen vacancies remain ferromagnetic, although the value of the exchange parameters J_{01}^{11} reduced from [5.8]meV in the non-relaxed case to [2.6]meV after relaxations. The critical temperature, estimated within the random phase approximation, is about [120]K in the relaxed geometry.

The most important question is why the relaxations of Zn atoms around the vacancy lead to such substantial changes of magnetic interactions. The Zn states are deep in the valence band and do not hybridize with the V states which are located close to the Fermi level (see Fig. 8). Relaxations of oxygen atoms were found to be very small and do not change magnetic properties of $(Zn_{1-x}V_x)O$. However, the hybridization between V 3*d* and oxygen 2*p* states is strongly affected by the relaxations of Zn atoms (see the partial DOS in Fig. 9), which is evidently crucial for the magnetic interactions in this system. Our analysis of the DOS and occupation numbers yields a significant increase of the hybridization between V 3*d* and O 2*p* states. This is governed by stronger *d*–*d* hybridization between Zn atoms moved towards the vacancy and, at the same time, due to a decrease of hybridization between these Zn 3*d* and O 2*p* states.

4.2 Mn-doped zirconia

In the wake of Dietl's prediction [68] that ZnO should become ferromagnetic when doped with a transition metal and the experimental discovery of room temperature ferromagnetism in Co-doped titania films, there has been considerable experimental and theoretical work on some other DMO. As well as a high T_C, a useful attribute of any DMO for a good spintronics material is a large spin polarization (difference between the majority and minority spin density of states at the Fermi energy). The material must also be easy to fabricate, stable and compatible with conventional semiconductors and metals. Based on state of the art *ab-initio* electronic structure calculations [73] we proposed that Mn-doped cubic zirconia, well-known both as a catalyst and also as synthetic diamond is a promising spintronics material.

Pure ZrO_2 is one of few high dielectric constant and wide-gap insulators and is known to be thermally stable on SiGe. It is being investigated as an insulating gate in complementary metal-oxide semiconductor field effect transistors. The cubic phase is stabilized at room temperature by the addition of 3 to 40 mol% MnO to ZrO_2 [74]. Our calculations show that manganese-stabilised cubic zirconia remains ferromagnetic to reasonably high temperatures. Epitaxial growth of zirconia thin films on Si, SiGe and Ge substrates is now easily achievable [75, 76] and of sufficient quality to be important for future low-leakage transistors with vertical channels. From the characterization of ZrO_2 on Si, SiGe and Ge it seems that ZrO_2 meets all requirements for incorporation into a field effect transistor device.

Thanks to the commercial applications much is known about cubic zirconia. The cubic phase of ZrO_2, which exists between 2370°C and the melting point, has the fluorite structure with each metal ion in regular 8-fold coordinated sites. When doped with other binary oxides, such as Y_2O_3 or MnO, the cubic phase of zirconia can be stabilised below 1000 K down to room temperature. Cubic zirconias are also well known as synthetic substitutes for diamond. For instance, Mn-ZrO_2 has green or violet colour due to Mn electronic states in the fundamental band gap of ZrO_2. Here the Mn impurities substitute some of the host Zr sites and up to 40% doping has been

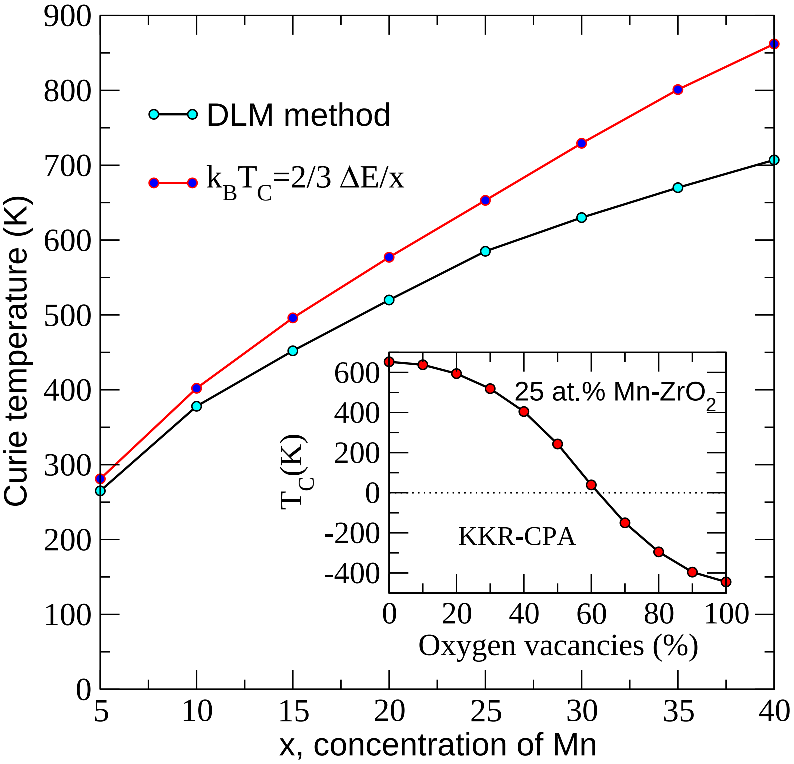

Figure 12: The dependence of T_C upon Mn concentration in cubic zirconia using KKR-CPA techniques and DLM theory. T_C extracted from the difference between the total energies of the ferromagnetic and paramagnetic states is also shown. Inset: The variation of T_C as a function of the number of unrelaxed oxygen vacancies, $4y$ (percentage per Mn impurity) where 0< y <0.25.

achieved [74].

The essential part of our study concerns the effects of thermally induced magnetic fluctuations upon the electronic structure and the estimate of T_C. The CPA is used also to handle both the local moment disorder as well as the location of the randomly distributed magnetic impurities. For a ferromagnet $k_BT_C = S^2(0)/3$. We complement these calculations with further ones based on the KKR technique, in which periodic boundary conditions are imposed on a 12-atom fluorite supercell. This allows us to study the effect of short-range order of the magnetic impurities.

Fig. 12 shows our estimates of T_C of $(Zr_{(1-x)}\ Mn_x)O_2$ for the range of concentrations x at experimental lattice constants using our KKR-CPA techniques and DLM theory. T_C rapidly increases to well above room temperature as x is raised above 5%. At 25% T_C is 570 K (the figure also shows the estimate of T_C from the difference in total energies of the ferromagnetic and paramagnetic DLM states). The spin-resolved DOS of Mn-ZrO$_2$ (Fig. 13) in its FM state shows a pronounced half-metallicity. Its origin comes from the Hund's rule that the majority spin $3d$ impurity states are fully occupied. The minority spin states lie partially in zirconia's fundamental band gap. For each spin, there are two impurity DOS peaks above the top of the valence band separated by the pseudogap, which can be associated with the e_g-t_{2g}-splitting expected from a simple ligand field model of the bonding in cubic ZrO$_2$.

Fig. 14 shows the dependence of the calculated T_C on volume and Mn concentration x. The lattice parameter of zirconia decreases from 5.11 Å to 5.044 Å at 30 at.% Mn [74]. The theoretical values (also in Fig. 14) are in reasonable agreement with the experiment, typically underesti-

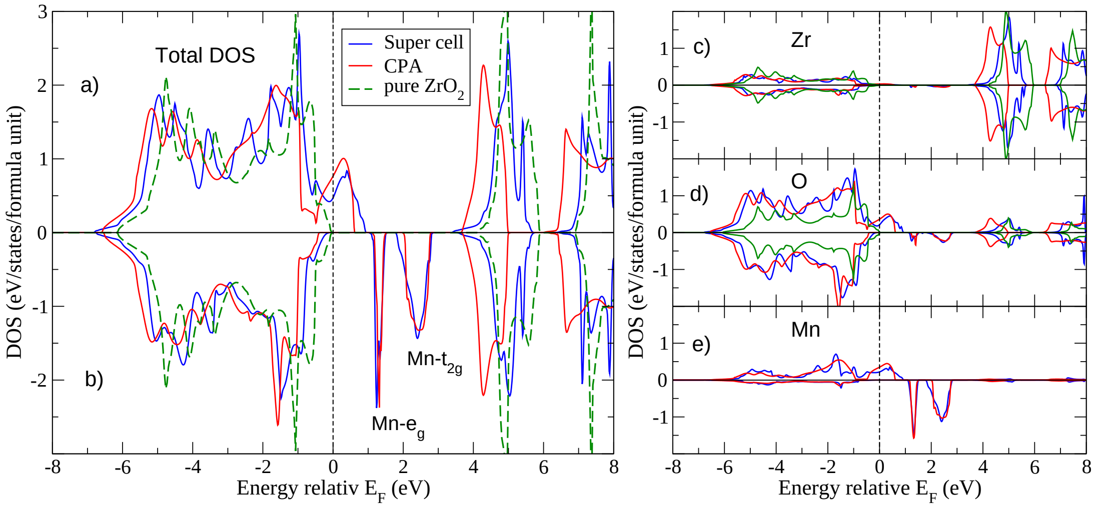

Figure 13: Panels (a) and (b): spin-resolved DOS of $Zr_{0.75}Mn_{0.25}O_2$ (super cell (blue solid line) and CPA (red solid line) and pure ZrO_2 (green dashed line)). Panels (c), (d) and (e): spin- and states-resolved DOS for $Zr_{0.75}Mn_{0.25}O_2$ for Zr, O and Mn respectively.

mating the equilibrium volume by ~5%. (The use of the generalised gradient correction to the LDA would result in better agreement whilst affecting our key conclusions for the magnetic properties.)

The important part of our investigation concerns the sensitivity of the magnetism in Mn-ZrO_2 to the presence of oxygen vacancies. The inset of Fig. 12, shows our KKR-CPA calculations of the T_C of 25% Mn-ZrO_2 as a function of the O vacancy concentration from the difference in total energies of the ferromagnetic and paramagnetic states. T_C remains high when there is up to one oxygen vacancy for every three Mn ($4y <33\%$). Beyond that T_C decreases near linearly so that when the number of vacancies approaches the number of Mn impurities ($4y >65\%$) the system is no longer ferromagnetic. For $4y{=}50\%$, the system, comparable to that of Y-stabilized zirconia where each pair of yttrium impurities creates one vacancy, should still be ferromagnetic and a half-metal. Consideration of both the oxidation state of the Mn-impurities and the number of extra electrons provided by this doping indicates that the number of oxygen vacancies in Mn-ZrO_2 should be less than in Y-ZrO_2 and T_C well above room temperature.

Therefore, the *ab initio* based theory anticipates that manganese stabilised cubic zirconia can become a room-temperature single-spin injector. The insulating wide gap of the host ZrO_2 plays no important role when the magnetic dopant level is high since the electronic density of states is completely spin polarised at the Fermi level. If this is true then the conductivity must be dominated by this metallic single-spin channel.

Very recently, it has been shown experimentally [77, 78] that nanosized 5-at.% Mn-doped ZrO_2 thin films grown on $LaAlO_3$ substrates can be ferromagnets with T_C above 400 K. The saturated magnetic moment measured there decreases as the Mn content increases. The authors suggest that intrinsic ferromagnetism is strongly associated with the cubic structure of Mn-doped ZrO2, and the Mn-Mn interactions via oxygen intermediates are important. No electrical conductivity was observed.

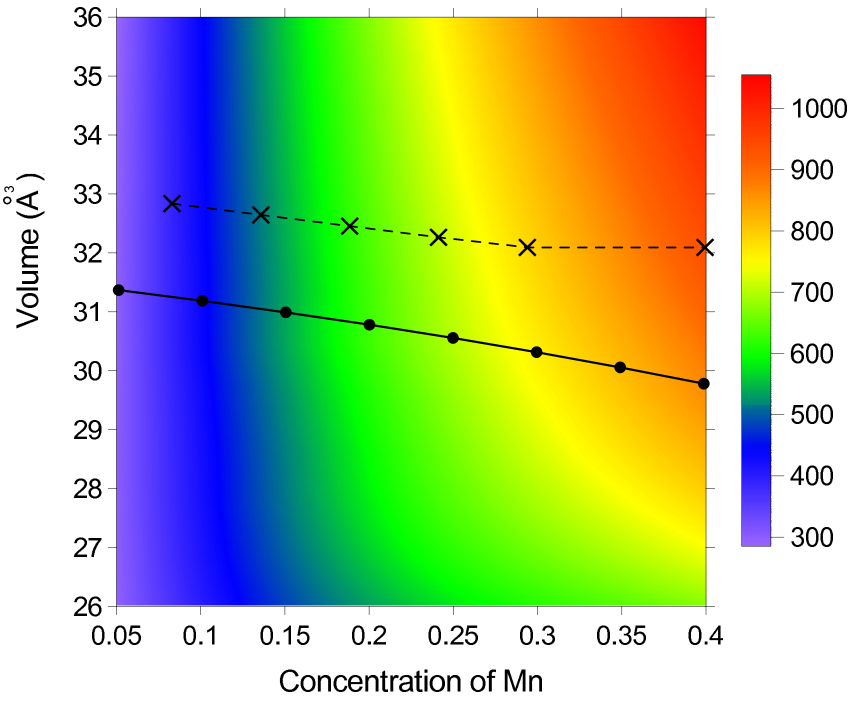

Figure 14: T$_C$ of $Zr_{1-x}Mn_xO_2$, calculated with the use of KKR-CPA, is plotted as a contour map versus Mn concentration and volume. The theoretical equilibrium volumes (solid line) obtained at each x are plotted together with the experimental data (dashed line).

4.3 Mn-doped HFO$_2$

Pure HfO$_2$ is being investigated as a high dielectric constant insulating gate for field effect transistor technology. Previously, Coey *et al.* [79] have reported that thin films of HfO$_2$ produced by pulsed-laser deposition on sapphire, yttria-stabilized ZrO$_2$ and silicon substrates show ferromagnetic magnetization curves with Curie temperature of the order of 400 K. On the basis of *ab initio* calculations [80] we suggested that Mn-doped cubic HfO$_2$ may match extremely demanding spintronics criteria. Although the upper limit of solubility of manganese in hafnia is unknown, it might be compatible with that of Mn-ZrO$_2$.

Using the KKR-CPA technique, the equilibrium volume of $Hf_{1-x}Mn_xO_2$ was calculated for several compositions between $0< x <0.5$. In Fig. 15, we plot the calculated T$_C$ as a function of x. The volume decreases with increasing x. When $x >5\%$ T$_C$ increases to well above room temperature. A similar effect was reported for Mn-ZrO$_2$ [73]. However, the T$_C$ value of Mn-HfO$_2$ increases more rapidly with the Mn concentration than that estimated for Mn-doped zirconia. For instance, at $x = 0.25$ the estimated T$_C$ of Mn-HfO$_2$ is about 30 K larger compared to that of Mn-ZrO$_2$. For $Hf_{0.75}Mn_{0.25}O_2$ we calculated the interatomic Heisenberg exchange parameters. The T$_C$ calculated within the mean field approximation is 682 K while the use of RPA yields T$_C$=578 K.

Until recently, the effect of the oxygen vacancy defects in ceramics on their possible high-T$_C$ ferromagnetism was not studied. To model the presence of oxygen vacancy in Mn-HfO$_2$ the CPA can be used. The inset of Fig. 15 illustrates the dependence of Curie temperature of 25% Mn-HfO$_2$ upon the number of oxygen vacancies δ. It is shown that the system is a room temperature ferromagnet when $\delta <1/8$. It means that to keep T$_C$ above 300 K the upper limit for the O vacancies accommodated in Mn-HfO$_2$ is one vacancy per two manganese atoms. Formally, it

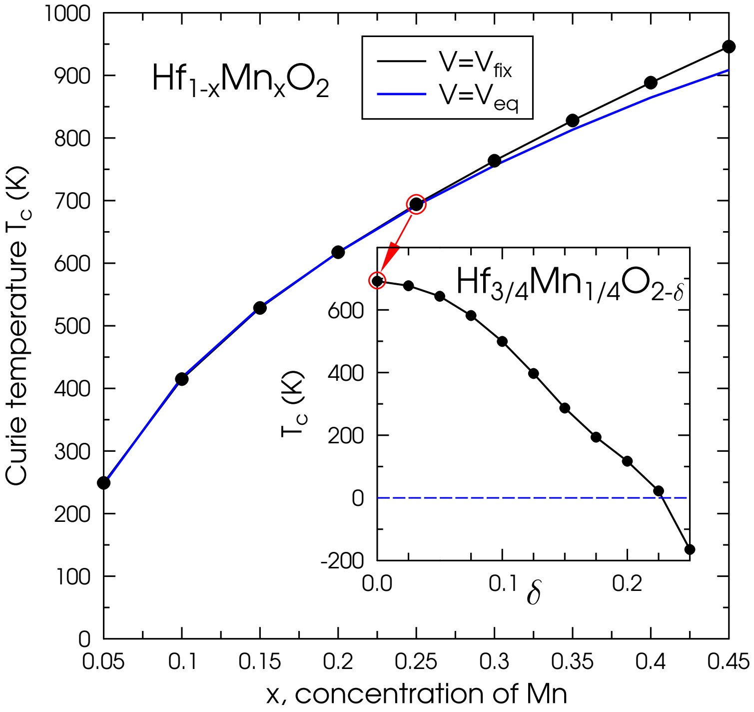

Figure 15: Curie temperature upon Mn concentration in $Hf_{1-x}Mn_xO_2$, calculated for equilibrium volumes using the KKR-CPA method. Inset: The variation of T_C for $Hf_{3/4}Mn_{1/4}O\delta$ as a function of the number of unrelaxed oxygen vacancies δ. The δ=1/8 corresponds to a half of the oxygen vacancy per manganese.

corresponds to the Mn 3^+ oxidation state. If $x < 0.25$ then the O vacancy limit becomes smaller. We suggest that the coexistence of Mn(IV) and Mn(III) in Mn-doped hafnia is essential for obtaining high T_C.

Another important property of Mn-HfO$_2$ from the spintronics point of view is its half-metallicity. Fig. 16 shows the electronic DOS calculated for the 25% Mn-HfO$_2$ composition, using both the supercell and CPA approaches. The spin-resolved DOS shows the metallic character for majority spin (Fig. 16a) and the band gap of ∼1eV for minority spin (Fig. 16b). Hence, the 25% Mn-HfO$_2$ as well as Mn-stabilized zirconia can be half-metallic at 0 K. The lowest unoccupied electronic states for the minority spin channel of 25% Mn-HfO$_2$ are composed by the Mn 3*d* states, namely, the e_g and t_{2g} subbands, which are separated from each other by the crystal field. Because of the well known strong localization of the e_g and t_{2g} states, it is unlikely that the half-metallic behavior of Mn-HfO$_2$ can be significantly affected at the finite temperatures. This makes this material very appealing.

The Mn magnetic moments calculated for x_{Mn}=0.25 using the CPA and supercell approaches are 3.35 μ_B and 3.41 μ_B, respectively. The total magnetization calculated per cell shows rather different values: 2.37 μ_B in the case of CPA and 2.99 μ_B when the 12-atom supercell is used. Hence, the induced magnetic moments are directed antiparallel to the Mn magnetic moment. It is clear that the widely used local CPA cannot properly treat the long-range interactions, which can play an important role in the system. The Mn magnetic moment weakly depends on x_{Mn} while it notably increases with the O vacancy concentration δ. For x_{Mn}=0.25 and δ=0.25 we obtain 4.21 μ_B on the Mn site and 4.69 μ_B per cell. It seems that at the presence of unrelaxed oxygen vacancy in Mn-HfO$_2$ some induced magnetic moments being aligned parallel to the Mn moment, contribute to the total magnetization. The sign of the O magnetic moments is negative between $0 < \delta < 0.5$ and then it vanishes at δ=0.5 while the Mn moment adopts its integer value of $4\mu_B$. We suggest that in search for high-T_C Mn-doped 4*d* oxides one must keep the number of oxygen vacancies below 1/8.

Thus, based on the *ab initio* aspects of our work, we anticipate that Mn stabilized cubic hafnia, $Hf_{1-x}Mn_xO_\delta$, can become a room temperature half-metallic ferromagnet when $x > 0.2$ and $\delta < 0.125$. This means that the Mn/Hf ratio is larger than 1:5 and, simultaneously, the ratio between the number of possible oxygen vacancies and Mn impurities must be less than 1:2, providing the coexistence of Mn(IV) and Mn(III) in the system.

In the context of experimental studies reported so far on such DMO thin films, as Mn-ZrO$_2$, it seems that the mechanism responsible for ferromagnetism is different from what was expected. Here the interface/surface defects and oxygen vacancies can be the source for magnetism. This stimulates further *ab initio* studies of a more stable DMO material.

5 Magnetic oxidic surfaces

The investigation of diluted magnetic oxides, of which some examples were presented in the previous section, is strongly connected to the study of surfaces of formally non-magnetic oxides. In fact, it is now believed that the experimentally observed defect-induced magnetism is mainly located at surface and interface regions [81], thereby explaining its tiny magnitude. There are

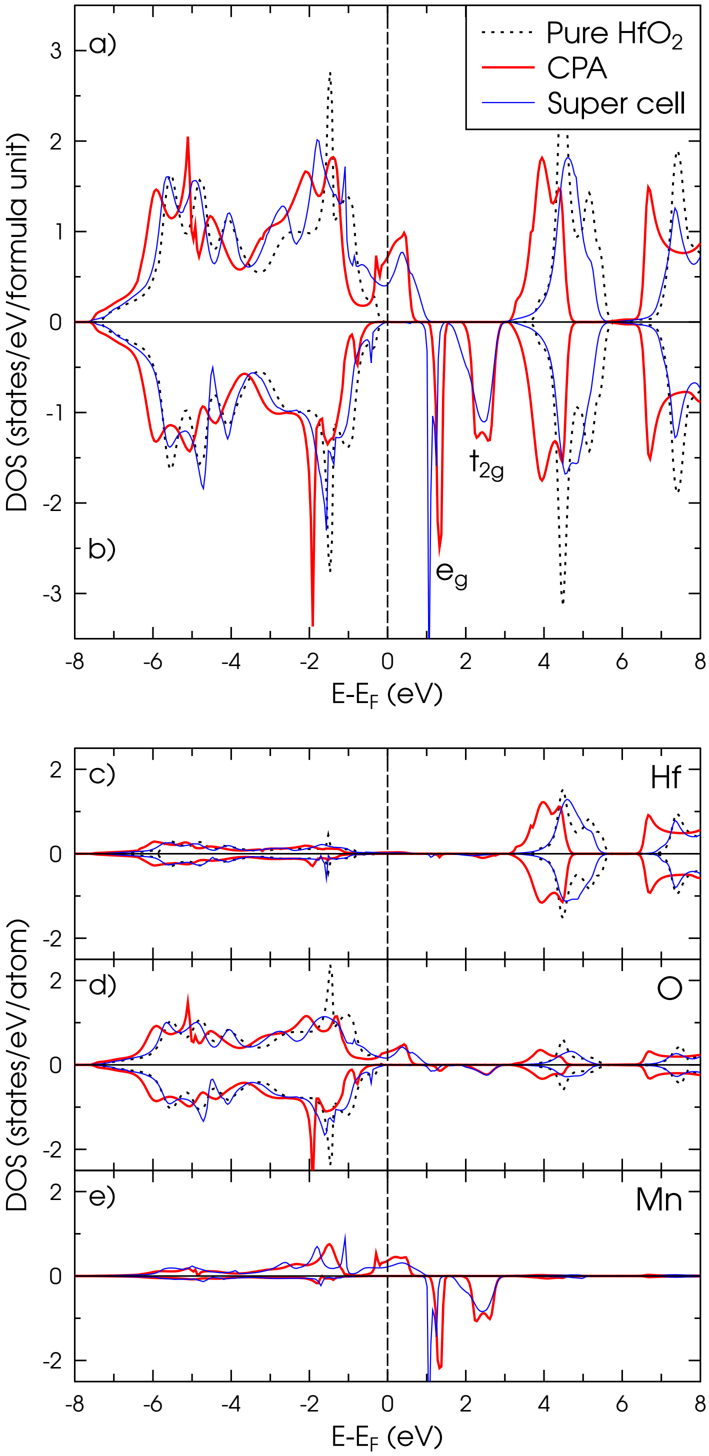

Figure 16: (a), (b) Spin-resolved DOS of $Hf_{3/4}Mn_{1/4}O_2$, calculated using the supercell and CPA approaches. The DOS of pure HfO_2 is shown for comparison. (c)-(e) The corresponding site-resolved DOS curves.

several reasons for this. For instance, foreign atoms and lattice defects are more likely to exist near surfaces due to a reduction of their formation energy in such regions. Moreover, surfaces are easier to access experimentally than bulk materials and can as well be manipulated more effectively. Finally, it is the surface itself which can create magnetism in materials, which are non-magnetic as bulk. This is caused by the occurrence of broken bonds, which often lead to structural or electronic reconstructions and to increased adsorption of foreign atoms, which in turn promote the formation of magnetic moments [82–85]. Their formation can be caused by localized electrons, but as well by localized holes. Ideally, these moments are coupled via a strong magnetic exchange that leads to magnetic order, such as ferromagnetism, at room temperature and above.

5.1 ZnO surfaces

One of the prototypes of such high temperature ferromagnetic oxides is ZnO. Using a multi-code approach as described above, we investigated its (0001) surface terminated with a full oxygen layer [86]. To describe the $3d$ electrons of Zn adequately we used Hubbard corrections with $U = 5.7$ eV within the pseudopotential approach and SIC applied to all $3d$ spin channels of Zn within KKR. The relaxed geometrical structure, shown in Figure 17, was obtained using SIESTA. As can be seen in Figure 17, the topmost O atom, O^1, is not found right on top of the uppermost Zn atom, Zn^1, but it relaxes into the three-fold fcc symmetric hollow site. This reduces the surface energy by ≈ 1 eV. Due to the only one out of four remaining Zn neighbours, there are 1.5 electron holes introduced and mainly localised at O^1. This can clearly be seen in Figure 18a). The holes exclusively localize in the minority spin channels, mainly in those of the p states of O^1 and O^2. Thus, the O-terminated (0001) ZnO surface is half-metallic. Due to hybridisation effects, a tiny fraction of the holes is also present at the Zn atoms near the surface. This results in a magnetisation distribution as shown in Figure 18b). Large magnetic moments are found at O^1 and O^2, the values of which are given in Table 4 in the first row. They

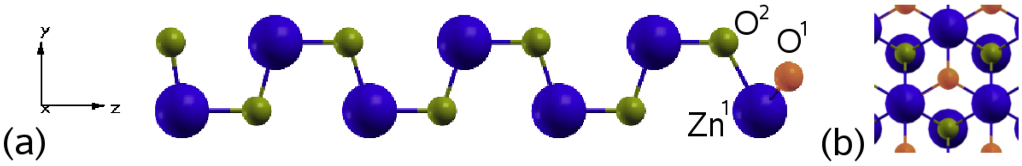

Figure 17: *(a)* The investigated ZnO slab unit cell (vacuum region not shown) in its ground state structure after relaxation, with oxygen (small yellow and orange) and zinc (big blue) atoms. The (0001) surface is on the right and is characterized by the topmost O atom in the three-fold coordinated hollow position, O^1, and the Zn and O atom underneath, labeled Zn^1 and O^2, respectively. *(b)* Top view of the (0001) surface.

Table 4: Magnetic moments (in μ_B) for the topmost layers of the (0001) surface. The layers are labeled according to Figure 17.

	O^1	Zn^1	O^2
MM (SIESTA)	0.94	0.01	0.53
MM (LSIC-KKR)	1.06	-0.06	0.42

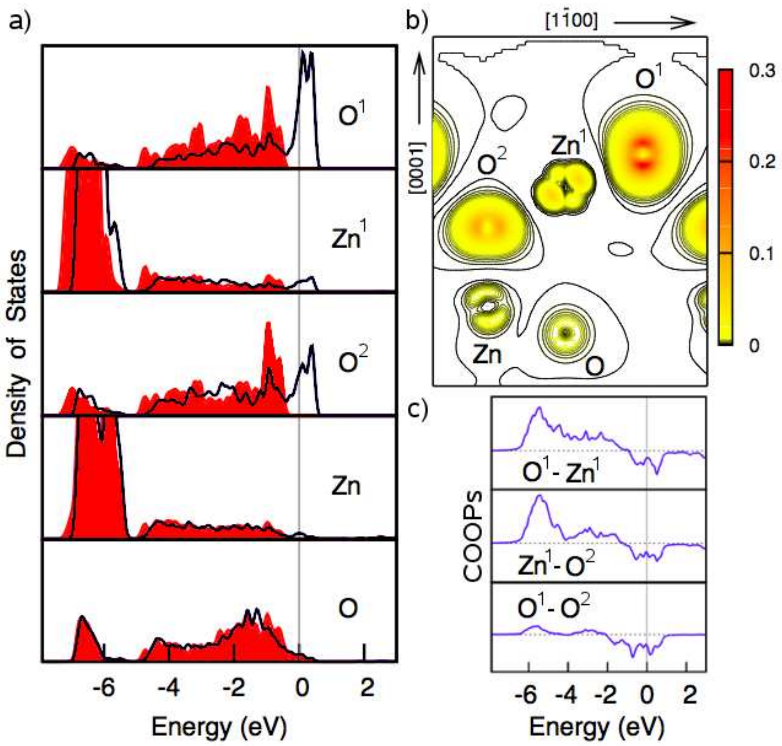

Figure 18: *a)* Spin resolved local DOS of the topmost layers of the O-ended (0001)-h surface. Red filled (black) values represent majority (minority) spin states. *b)* Spin density distribution of the (0001)-h surface. *c)* COOPs between the atoms in the first three layers. Energies are relative to E_F.

demonstrate the strong localization at the two topmost oxygen atoms. Figure 18c) shows the crystal orbital overlap populations (COOPs) between the first two layers (O^1 and Zn^1; Zn^1 and O^2) and between the two O atoms O^1 and O^2. Being a measure for the amount of hybridisation between two atoms the COOPs not only show a strong coupling between the first three layers, but they also indicate a significant direct electronic overlap between O^1 and O^2. The reason for this is, on the one hand, the relatively close distance between these two atoms (2.30 versus 3.25 [Å] for nearest neighbour O atoms in ZnO bulk) and, on the other hand as can be seen in Figure 17, the fact that no Zn atom is between them. This suggests, that the magnetic moment at O^2 is rather induced from O^1 and that its localization is not very strong.

Using the KKR approach and Equation (10) to determine the Heisenberg exchange parameters J_{ij}, we find strong magnetic interaction at the surface. The strength of the first interaction pairs are visualized in Figure 19. They are strongly ferromagnetic and demonstrate that the interaction is significant only if there is at least one O^1 involved. This supports the rather induced character of the magnetic moment at O^2. Any interaction involving other atoms than these is negligibly small. Using the calculated J_{ij} in Monte Carlo simulations yields a Curie temperature above 300 K, the exact value depends on the assumed value anisotropy. This means that the O-terminated ZnO (0001) surface as shown in Figure 17 exhibits ferromagnetism at room temperature.

It had been pointed out before that localized electron holes may not be adequately described by standard LDA or GGA [87–89]. Therefore, we also investigated the necessity of applying SIC

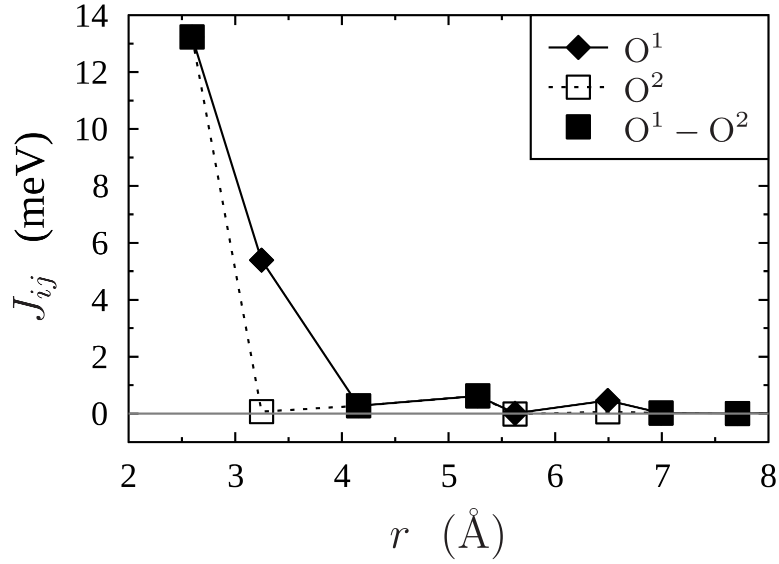

Figure 19: J_{ij} of pairs containing O^1 (◆) or O^2 (□), respectively, depending on the distance. The full black squares (■) mark the J_{ij} between one O^1 and one O^2 atom.

to the p states of O, in addition to the SIC treatment of the Zn $3d$ states. We did indeed find that the global SIC ground state corresponds to the one in which all three majority p electrons of O^1 are SI-corrected, together with SIC on the $3d$ orbitals. The resulting electronic structure does not differ significantly from that presented here. The localization of the electrons at O^1 and, thus, the magnitude of the magnetic moment at O^1, too, is increased at the expense of the magnetic moment at O^2. The enhancement of the J_{ij} due to the increased moments (note, that the magnitude of the spin vectors is implicitly included in the J's) and their weakening due to the reduced delocalization and, accordingly, electronic overlap, more or less even out. Thus, the Curie temperature of the system with SIC additionally applied to the majority p states of $O^1$is almost the same as that of the system with SIC only at the Zn $3d$ states.

5.2 $BaTiO_3$(001) surface

Another possibly spin-polarized surface of a non-magnetic system was investigated recently in the work of Meyerheim *et al.* [90]. In this study, the (001) surface of $BaTiO_3$, which is a prototypical ferroelectric system, was modified using a mild Ar^+ ion sputtering followed by two annealing cycles of 20 min each at a temperature of about 850-900°C. This leads to a 2×1 surface reconstruction with a double layer TiO_2 termination. The crystalline structure of the surface was investigated using surface x-ray diffraction (SXRD), which can provide precise atomic positions and the chemical composition of thin films [35].

The structure model, elucidated from this experiment, is shown in Fig. 20. In this model, the Ti-atom originally located at $(\frac{1}{2}, 0)$ (see dashed circles in Fig. 20(a)) is shifted to the position $(1, 1)$ in the center of the unit cell. This atom is labeled as 5. An oxygen atom (4) was found on above the Ti atom (5). The structure model is shown in perspective view in Fig. 20(c). The Ti atom 5, which is above the third layer Ba atom, is located [0.53]Å below the bulk truncated surface to bind to four O atoms in the second layer (7, 8, and equivalent ones) at a distance of

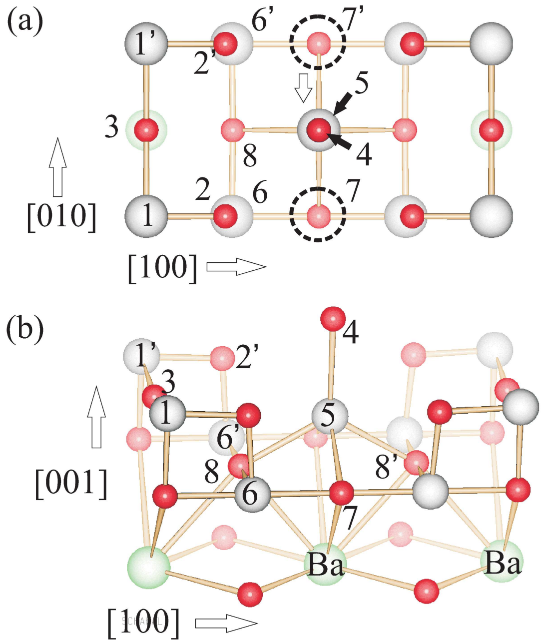

Figure 20: (a): Structure model of the (2×1) reconstructed unit cell projected along [001]. Atoms within the two top TiO$_2$ layers are labelled from 1-8. O and Ti atoms are represented by red and grey spheres, respectively. Dashed circles indicate the positions of Ti atom 5 in the unreconstructed (1×1) structure, which is shifted to the position (1/2, 1/2) as indicated by the arrow. (b): Perspective side view of the structure. Interatomic distances in Ångstrom units: 1-2:1.82, 1-3:2.01, 2-6:1.88, 8-6:2.00, 5-4:2.30, 5-8:2.29, 7-6:2.01, Ba-O (in-plane): 2.82, Ba-O (out of plane): 3.09.

[2.29]±[0.15]Å. The fifth O atom (4) is located on top at [2.30]±[0.15]Å. In consequence, Ti atom 5 resides in the center of a tetragonal pyramid. Some interatomic distances are listed in the caption of Fig. 20(b). An overall expansion of the spacing between the second TiO$_2$ layer and the third (bulk like) BaO layer was found in the range of 5%.

Further, we investigated the electronic and magnetic properties of the (2×1) BaTi$_3$ surface within the density functional theory in the local density approximation using a Korringa-Kohn-Rostoker Green-function method, which is specially designed for semi-infinite layered systems [72]. The most important result is that the BaTiO$_3$(001)-(2 × 1) surface is metallic and magnetic within the DFT calculations independent on the choice of the functional. The VASP code provides similar results.

Fig. 21 compares the spin-resolved density of states (DOS) of (a) TiO2 terminated BaTiO$_3$(001)-(1 × 1) and (b) BaTiO$_3$(001)-(2 × 1) surfaces. The DOS of the BaTiO$_3$(001)-(1 × 1) surface 21(a) exhibits a quasimetallic behavior which is in agreement with the previous calculations. This kind of metallic character might be destroyed by the presence of impurities and imperfections leading to an insulating surface. The band structure below the Fermi level comprises hybridized Ti 3*d* and O 2*p* states, while bands above the Fermi level in the 3-5 eV range are identified as antibonding Ti 3*d* states. Since the DOS of both Ti and O atoms exhibit an almost identical distribution, a very strong hybridization between Ti 3*d* and O 2*p* states is inferred.

The situation is completely different in the case of the BaTiO$_3$(001)-(2 × 1) surface 21(b), where a strong metallicity is observed. It is mainly a consequence of the hybridization between the Ti

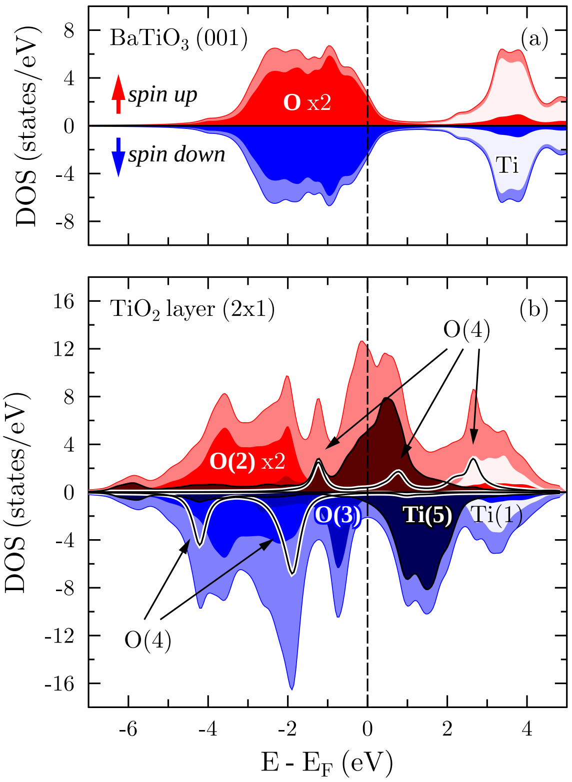

Figure 21: Calculated spin resolved density of states for BaTiO$_3$(001)-(1x1) (a) and BaTiO$_3$(001)-(2x1) (b). Atomic labelling corresponds to the structure model in Fig. 20(a),(b)

atom (5) with the surrounding oxygen atoms involving a shift of the (previously unoccupied) Ti-3d states to the Fermi level corresponding to a charge transfer to the Ti atom (5). Simultaneously, we found that, as a result of the low coordination and reduced symmetry, a narrowing of the DOS occurs involving partially unsaturated 2p states in the case of the O atoms (3) and (4). In turn this leads to high local magnetic moments.

Fig. 22 shows the calculated spin density contour plot in the plane defined by the [100] and the [001] direction. In detail, the atoms Ti (5) and O (4) are antiferromagnetically coupled characterized by magnetic moments of [1.3]μ_B and [2.0]μ_B, respectively. The magnetic interaction in the Ti(5)-O(4) bond is strongly localized. By contrast, O atoms (3) form a magnetic chain along [010] with local magnetic moments of [0.5]μ_B. The total energy calculations also reveal that the surface is magnetic with the total magnetic moment of [1.5]μ_B.

Thus, our structural analysis of the BaTiO$_3$(001)-(2×1) reconstruction has identified an atomic arrangement not considered so far for (001) oriented perovskite surfaces. The most remarkable unit is a Ti atom in a tetragonal pyramidal environment. This unique structural motif causes symmetry breaking, localization of the electronic states, and charge transfer to the central Ti atom (5) from surrounding oxygen atoms, the latter being directly related to the shift of the otherwise unoccupied 3d states to the Fermi level. This leads to the metalization and magnetization which is now identified as an intrinsic property of the surface. We infer that this metalization also contributes to the stabilization of the reconstruction related to the depolarization of the surface.

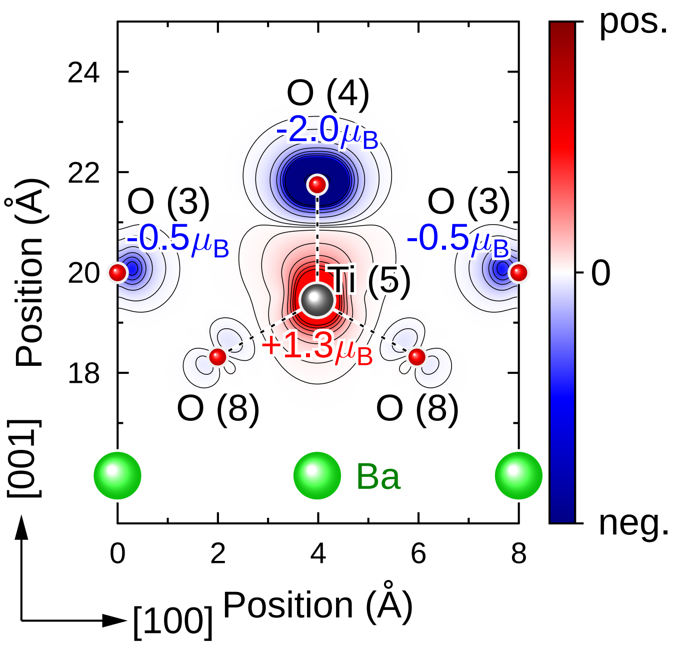

Figure 22: Spin density and magnetic moments calculated for $BaTiO_3(001)$-(2×1).

6 Summary

In this Highlight we presented our approach for a first-principles design of magnetic complex oxides, which is based on the density functional theory and is appropriate for systems with itinerant and localized electrons. In this approach, itinerant Bloch electronic states are described within the local spin density approximation, while strongly localized electrons are treated by means of the self-interaction correction method. The crystalline structure can be either adopted from experiments or obtained using pseudopotential codes, which are well designed for total energy calculations. Further information about the structure and chemical composition can be elucidated from first-principles simulations of observable properties, e.g. as XAS and XMCD spectra, and their fit to experimental results. A particular feature of our approach is a proper description of magnetic properties such as exchange interactions, spin excitations and transition temperatures. For this, we apply a Green function method within the multiple scattering theory. The Green function is used to calculate magnetic and paramagnetic susceptibility, which provides spin excitations, their lifetime and the strength of magnetic interactions. In this Highlight, we demonstrated the efficiency of our approach for a study of electronic and magnetic properties of several complex magnetic systems such as transition metal oxides, diluted magnetic oxides and spin-polarized surfaces of non-magnetic oxidic materials. According to our study, the TMO's can be adequately described within the self-interaction correction method, which provides a proper description of strongly correlated $3d$ electrons of transition metals in these materials. The calculated exchange constants, magnons and transition temperatures of TMO'S are found to be in a good agreement with experiment. Moreover our description of the paramagnetic state of these materials in terms of disordered local moments shows how the band gap persists as the antiferromagnetic order is lost above the Néel temperature.

Our approach works well for diluted magnetic oxides. In particular we described magnetic properties of zirconia doped with manganese and predicted a high transition temperature in this system, which was later confirmed experimentally. For (Zn,V)O diluted magnetic oxides we were able to fit experimental XAS and XMCD spectra and, by doing so, identify the chemical composition of the alloy. Using the elucidated structure, we explained the electronic and magnetic properties of these compounds.

Another field of applications for our approach concerned so-called *p* magnetism, which can occur due to broken *p* bonds in oxides. The broken bonds can arise because of defects or surface termination and promote the formation of magnetic moments. This can lead to magnetic ordering on the surface provided that long-ranged exchange interactions between these moments occur.

The future progress in the theoretical design of oxides will require a substantial development both in the formal and corresponding numerical areas. One of the promising ways to take is the so called GW method of Hedin [8]. In this context, even the simplest random phase approximation yields a substantial improvement of the values of the band gaps in simple semiconductors (Si, Ge), and one expects that also the values for oxides could be correctly predicted along this line. Such development would constitute the desired first-principles description of the problem not involving adjustable parameters as in the case of the LDA+U. One could mention that the first-principles SIC corrected ground state could be taken as a better starting point for the subsequent GW treatment. However, the GW of oxides is a more complex one that for simple semiconductors, as the primitive cells feature normally many more atoms. In addition, a proper treatment of crystal imperfections (surfaces, interfaces, defects, etc.) would require a routine treatment of systems involving tens to hundred non-equivalent atoms. At the moment the associated computational cost excludes a direct GW application for many systems of interest mentioned in the summary. The main bottleneck here is primarily the computation and memory storage of dielectric matrices. With our experience in the linear response theory, the problem is currently being addressed. Finally, it would be desirable to include in the GW formalism physics beyond the simple RPA, i.e. to include the so-called vertex corrections. An example of such an effect is the magnon-electron scattering which is believed to influence strongly properties of magnetic materials. It is, at the moment, another area of intensive research.

References

[1] P. Hohenberg and W. Kohn. Inhomogeneous electron gas. *Phys. Rev.*, 136:B864–B871, 1964.

[2] W. Kohn and L. J. Sham. Self-consistent equations including exchange and correlation effects. *Phys. Rev.*, 140:A1133–A1138, 1965.

[3] John P. Perdew, J. A. Chevary, S. H. Vosko, Koblar A. Jackson, Mark R. Pederson, D. J. Singh, and Carlos Fiolhais. Atoms, molecules, solids, and surfaces: Applications of the generalized gradient approximation for exchange and correlation. *Phys. Rev. B*, 46:6671–6687, 1992.

[4] John P. Perdew, Kieron Burke, and Matthias Ernzerhof. Generalized gradient approximation made simple. *Phys. Rev. Lett.*, 77:3865–3868, 1996.

[5] J. P. Perdew and Alex Zunger. Self-interaction correction to density-functional approximations for many-electron systems. *Phys. Rev. B*, 23:5048–5079, 1981.

[6] Vladimir I. Anisimov, Jan Zaanen, and Ole K. Andersen. Band theory and mott insulators: Hubbard U instead of stoner I. *Phys. Rev. B*, 44:943–954, 1991.

[7] Axel D. Becke. A new mixing of hartree–fock and local density-functional theories. *The Journal of Chemical Physics*, 98:1372–1377, 1993.

[8] Lars Hedin. New method for calculating the one-particle green's function with application to the electron-gas problem. *Phys. Rev.*, 139:A796–A823, 1965.

[9] Antoine Georges, Gabriel Kotliar, Werner Krauth, and Marcelo J. Rozenberg. Dynamical mean-field theory of strongly correlated fermion systems and the limit of infinite dimensions. *Rev. Mod. Phys.*, 68:13, 1996.

[10] J. Korringa. On the calculation of the energy of a bloch wave in a metal. *Physica*, 13:392–400, 1947.

[11] W. Kohn and N. Rostoker. Solution of the schrödinger equation in periodic lattices with an application to metallic lithium. *Phys. Rev.*, 94:1111, 1954.

[12] O. Krogh Andersen. Linear methods in band theory. *Phys. Rev. B*, 12:3060–3083, 1975.

[13] B.L. Gyorffy and M. J. Stott. *Theory of Soft X-Ray Emission from Alloys*, chapter Theory of Soft X-Ray Emission from Alloys, pages 385–402. London and NY: Acad. Press, 1973.

[14] Erich Runge and E. K. U. Gross. Density-functional theory for time-dependent systems. *Physical Review Letters*, 52:997–1000, 1984.

[15] E. K. U. Gross and Walter Kohn. Local density-functional theory of frequency-dependent linear response. *Physical Review Letters*, 55:2850–2852, 1985.

[16] Takeo Izuyama, Duk-Joo Kim, and Ryogo Kubo. Band theoretical interpretation of neutron diffraction phenomena in ferromagnetic metals. *Journal of the Physical Society of Japan*, 18:1025–1042, 1963.

[17] R Kubo. The fluctuation-dissipation theorem. *Reports on Progress in Physics*, 29:255, 1966.

[18] Paweł Buczek, Arthur Ernst, and Leonid M. Sandratskii. Different dimensionality trends in the landau damping of magnons in iron, cobalt, and nickel: Time-dependent density functional study. *Phys. Rev. B*, 84:174418, 2011.

[19] L. Gyorffy, B. J. Pindor, A. J. Staunton, M. Stocks, G. and H. Winter. A first-principles theory of ferromagnetic phase transitions in metals. *Journal of Physics F: Metal Physics*, 15:1337, 1985.

[20] J. Staunton, B. L. Gyorffy, A. J. Pindor, G. M. Stocks, and H. Winter. Electronic structure of metallic ferromagnets above the curie temperature. *Journal of Physics F: Metal Physics*, 15:1387, 1985.

[21] J. B. Staunton, J. Poulter, B. Ginatempo, E. Bruno, and D. D. Johnson. Incommensurate and commensurate antiferromagnetic spin fluctuations in cr and cr alloys from ab initio dynamical spin susceptibility calculations. *Phys. Rev. Lett.*, 82:3340–3343, 1999.

[22] J. B. Staunton, J. Poulter, B. Ginatempo, E. Bruno, and D. D. Johnson. Spin fluctuations in nearly magnetic metals from ab initio dynamical spin susceptibility calculations: Application to pd and $cr_{95}v_5$. *Phys. Rev. B*, 62:1075–1082, 2000.

[23] I. D. Hughes, M. Däne, A. Ernst, W. Hergert, M. Lüders, J. Poulter, J. B. Staunton, A. Svane, Z. Szotek, and W. M. Temmerman. Lanthanide contraction and magnetism in the heavy rare earth elements. *Nature*, 446:650–653, 2007.

[24] S. V. Halilov, H. Eschrig, A. Y. Perlov, and P. M. Oppeneer. Adiabatic spin dynamics from spin-density-functional theory: Application to Fe, Co, and Ni. *Phys. Rev. B*, 58:293, 1998.

[25] V. P. Antropov, B. N. Harmon, and A. N. Smirnov. Aspects of spin dynamics and magnetic interactions. *Journal of Magnetism and Magnetic Materials*, 200:148–166, 1999.

[26] A. I. Liechtenstein, M. I. Katsnelson, V. P. Antropov, and V. A. Gubanova. Local spin density functional approach to the theory of exchange interactions in ferromagnetic metals and alloys. *Journal of Magnetism and Magnetic Materials*, 67:65–74, 1987.

[27] L. M. Sandratskii. Noncollinear magnetism in itinerant-electron systems: theory and applications. *Advances in Physics*, 47:91–160, 1998.

[28] O. Grotheer, C. Ederer, and M. Fähnle. Fast *ab initio* methods for the calculation of adiabatic spin wave spectra in complex systems. *Phys. Rev. B*, 63:100401, 2001.

[29] P. Strange, A. Svane, W. M. Temmerman, Z. Szotek, and H. Winter. Understanding the valency of rare earths from first-principles theory. *Nature*, 399:756, 1999.

[30] W. M. Temmerman, A. Svane, Z. Szotek, and H. Winter. *Electronic Density Functional Theory: Recent Progress and New Directions*, chapter Applications of Self-Interaction Corrections to Localized States in Solids, page 327. Plenum, New York, 1998.

[31] A. Svane and O. Gunnarsson. Transition-metal oxides in the self-interaction–corrected density-functional formalism. *Phys. Rev. Lett.*, 65:1148–1151, 1990.

[32] Z. Szotek, W. M. Temmerman, and H. Winter. Application of the self-interaction correction to transition-metal oxides. *Phys. Rev. B*, 47:4029–4032, 1993.

[33] M. Lüders, A. Ernst, M. Däne, Z. Szotek, A. Svane, D. Ködderitzsch, W. Hergert, B. L. Györffy, and W. M. Temmerman. Self-interaction correction in multiple scattering theory. *Phys. Rev. B*, 71:205109, 2005.

[34] V. V. Nemoshkalenko, A. E. Krasovskii, V. N. Antonov, Vl. N. Antonov, U. Fleck, H. Wonn, and P. Ziesche. The relativistic linear muffin-tin orbital method application to au. *physica status solidi (b)*, 120:283–296, 1983.

[35] R. Feidenhans'l. Surface structure determination by x-ray diffraction. *Surface Science Reports*, 10:105–188, 1989.

[36] G. Kresse and J. Furthmüller. Efficiency of ab-initio total energy calculations for metals and semiconductors using a plane-wave basis set. *Computational Materials Science*, 6:15–50, 1996.

[37] G. Kresse and J. Furthmüller. Efficient iterative schemes for ab initio total-energy calculations using a plane-wave basis set. *Phys. Rev. B*, 54:11169–11186, 1996.

[38] I. D. Hughes, M. Däne, A. Ernst, W. Hergert, M. Lüders, J. B. Staunton, Z. Szotek, and W. M. Temmerman. Onset of magnetic order in strongly-correlated systems from ab initio electronic structure calculations: application to transition metal oxides. *New Journal of Physics*, 10:063010, 2008.

[39] M. Däne, M. Luders, A. Ernst, D. Kodderitzsch, W. M. Temmerman, Z. Szotek, and W. Hergert. Self-interaction correction in multiple scattering theory: application to transition metal oxides. *Journal of Physics: Condensed Matter*, 21:045604, 2009.

[40] G. Fischer, M. Däne, A. Ernst, P. Bruno, M. Lüders, Z. Szotek, W. M. Temmerman, and W. Hergert. Exchange coupling in transition metal monoxides: Electronic structure calculations. *Phys. Rev. B*, 80:014408, 2009.

[41] S. Sasaki, K. Fujino, Y. Takéuchi, and R. Sadanaga. On the estimation of atomic charges by the X-ray method for some oxides and silicates. *Acta Crystallographica Section A*, 36:904–915, 1980.

[42] G. Albanese, A. Deriu, J. E. Greedan, M. S. Seehra, K. Siratori, and H. P. J. Wijn. *Landolt-Börnstein, New Series III/27g: Magnetic Properties of Non-Metallic Inorganic Compounds Based on Transition Elements: Various Other Oxides*. Berlin: Springer, 1992.

[43] Helmer Fjellvåg, Fredrik Grønvold, Svein Stølen, and Børn Hauback. On the crystallographic and magnetic structures of nearly stoichiometric iron monoxide. *Journal of Solid State Chemistry*, 124:52–57, 1996.

[44] N. G. Schmahl and G. F. Eikerling. über kryptomodifikationen des cu(ii)-oxids. *Zeitschrift für Physikalische Chemie*, 62:268–279, 1968.

[45] N. G. Schmahl, J. Barthel, and G. F. Eikerling. Röntgenographische untersuchungen an den systemen mgo-cuo und nio-cuo. *Zeitschrift für anorganische und allgemeine Chemie*, 332:230–237, 1964.

[46] D. C. Khan and R. A. Erickson. Magnetic form factor of co^{++} ion in cobaltous oxide. *Phys. Rev. B*, 1:2243–2249, 1970.

[47] H.K. Bowen, D. Adler, and B.H. Auker. Electrical and optical properties of feo. *Journal of Solid State Chemistry*, 12:355–359, 1975.

[48] Bong-soo Kim, Sayong Hong, and David W. Lynch. Inverse-photoemission measurement of iron oxides on polycrystalline fe. *Phys. Rev. B*, 41:12227–12229, 1990.

[49] G. A. Sawatzky and J. W. Allen. Magnitude and origin of the band gap in nio. *Phys. Rev. Lett.*, 53:2339–2342, 1984.

[50] G. E. Kugel, B. Hennion, and C. Carabatos. Low-energy magnetic excitations in wustite ($Fe_{1-x}O$). *Phys. Rev. B*, 18(3):1317, 1978.

[51] J. B. Goodenough. *Magnetism and the Chemical Bond.* John Wiley & Sons, New York, 1993.

[52] S. V. Tyablikov. *Methods of Quantum Theory of Magnetism.* Plenum Press, New York, 1967.

[53] Philip W. Anderson. *Theory of Magnetic Exchange Interactions: Exchange in Insulators and Semiconductors*, volume 14 of *Solid State Physics.* Academic Press, New York, 1963.

[54] G. Pepy. Spin waves in mno; from 4k to temperatures close to t_n. *J. Phys. Chem. Sol.*, 35, 1974. 47.

[55] K. Tomiyasu and S. Itoh. Magnetic excitations in coo. *J. Phys. Soc. Jpn.*, 75(8):084708, 2006. 43.

[56] M. D. Rechtin and B. L. Averbach. Long-range magnetic order in coo. *Phys. Rev. B*, 6(11):4294–4300, Dec 1972.

[57] R. Shanker and R. A. Singh. Analysis of the exchange parameters and magnetic properties of nio. *Phys. Rev. B*, 7(11):5000–5005, Jun 1973.

[58] M.T. Hutchings and E.J. Samuelson. Measurement of spin-wave dispersion in nio by inelastic neutron scattering and its relation to magnetic properties. *Phys. Rev. B*, 6:3447, 1972.

[59] Andrew L. Goodwin, Martin T. Dove, Matthew G. Tucker, and David A. Keen. Mno spin-wave dispersion curves from neutron powder diffraction. *Phys. Rev. B*, 75(7):075423, 2007.

[60] K. Sato, L. Bergqvist, J. Kudrnovský, P. H. Dederichs, O. Eriksson, I. Turek, B. Sancyal, G. Bouzerar, H. Katayama-Yoshida, V. A. Dinh, T. Fukushima, H. Kizaki, and R. Zeller. First-principles theory of dilute magnetic semiconductors. *Rev. Mod. Phys.*, 82:1633–1690, 2010.

[61] I. S. Elfimov, S. Yunoki, and G. A. Sawatzky. Possible path to a new class of ferromagnetic and half-metallic ferromagnetic materials. *Phys. Rev. Lett.*, 89:216403, 2002.

[62] J.M.D. Coey. Dilute magnetic oxides. *Current Opinion in Solid State and Materials Science*, 10:83–92, 2006.

[63] T. Dietl, T. Andrearczyk, A. Lipińska, M. Kiecana, Maureen Tay, and Yihong Wu. Origin of ferromagnetism in $zn_{1-x}co_xO$ from magnetization and spin-dependent magnetoresistance measurements. *Phys. Rev. B*, 76:155312, 2007.

[64] L. Petit, T. Schulthess, A. Svane, Z. Szotek, W. Temmerman, and A. Janotti. Electronic structure of transition metal impurities in p-type zno. *Physical Review B*, 73:045107, 2006.

[65] L. Petit, T. Schulthess, A. Svane, W. Temmerman, Z. Szotek, and A. Janotti. Valency configuration of transition metal impurities in zno. *Journal of Electronic Materials*, 35:556–561, 2006.

[66] O. Madelung. *Semiconductors: Data Handbook*. Berlin: Springer-Verlag, 2004.

[67] D. A. Bonnell, G. S. Rohrer, and R. H. French. *J. Vac. Sci. Technol. B*, 9:551, 1991.

[68] T. Dietl, H. Ohno, F. Matsukura, J. Cibert, and D. Ferrand. Zener model description of ferromagnetism in zinc-blende magnetic semiconductors. *Science*, 287:1019–1022, 2000.

[69] M. Joseph, H. Tabata, and T. Kawai. *Jpn. J. Appl. Phys., Part 2*, 38:L1205, 1999.

[70] S. H. Liu, H. S. Hsu, C. R. Lin, C. S. Lue, and J. C. A. Huang. Effects of hydrogenated annealing on structural defects, conductivity, and magnetic properties of v-doped zno powders. *Applied Physics Letters*, 90(22):222505, 2007.

[71] Y. Ishida, J. I. Hwang, M. Kobayashi, Y. Takeda, K. Mamiya, J. Okamoto, S.-I. Fujimori, T. Okane, K. Terai, Y. Saitoh, Y. Muramatsu, A. Fujimori, A. Tanaka, H. Saeki, T. Kawai, and H. Tabata. Soft x-ray magnetic circular dichroism study of weakly ferromagnetic zni$_{1-x}$v$_x$o thin film. *Applied Physics Letters*, 90:022510, 2007.

[72] M. Luders, A. Ernst, W. M. Temmerman, Z. Szotek, and P. J. Durham. Ab initio angle-resolved photoemission in multiple-scattering formulation. *Journal of Physics: Condensed Matter*, 13:8587–8606, 2001.

[73] S. Ostanin, A. Ernst, L. M. Sandratskii, P. Bruno, M. Däne, I. D. Hughes, J. B. Staunton, W. Hergert, I. Mertig, and J. Kudrnovský. Mn-stabilized zirconia: From imitation diamonds to a new potential high-t_C ferromagnetic spintronics material. *Phys. Rev. Lett.*, 98:016101, 2007.

[74] M. Lajavardi, D. J. Kenneya, and S. H. Lind. Time-resolved phase transitions of the nanocrystalline cubic to submicron monoclinic phase in mn2o3-zro2. *Journal of the Chinese Chemical Society*, 47:1055–1063, 2000.

[75] S. J. Wang, A. C. H. Huan, Y. L. Foo, J. W. Chai, J. S. Pan, Q. Li, Y. F. Dong, Y. P. Feng, and C. K. Ong. Energy-band alignments at zro[sub 2]/si, sige, and ge interfaces. *Applied Physics Letters*, 85:4418–4420, 2004.

[76] J. Okabayashi, S. Toyoda, H. Kumigashira, M. Oshima, K. Usuda, M. Niwa, and G. L. Liu. Chemical reaction and metallic cluster formation by annealing-temperature control in zro[sub 2] gate dielectrics on si. *Applied Physics Letters*, 85:5959–5961, 2004.

[77] Nguyen Hoa Hong, Chul-Kwon Park, A.T. Raghavender, Antoine Ruyter, Ekaterina Chikoidze, and Yves Dumont. High temperature ferromagnetism in cubic mn-doped zro2 thin films. *Journal of Magnetism and Magnetic Materials*, 324:3013–3016, 2012.

[78] Nguyen Hoa Hong, C.-K. Park, A. T. Raghavender, O. Ciftja, N. S. Bingham, M. H. Phan, and H. Srikanth. Room temperature ferromagnetism in monoclinic mn-doped zro[sub 2] thin films. *Journal of Applied Physics*, 111:07C302, 2012.

[79] J. M. D. Coey, M. Venkatesan, and C. B. Fitzgerald. Donor impurity band exchange in dilute ferromagnetic oxides. *Nature Materials*, 4:173–179, 2005.

[80] I.V. Maznichenko, S. Ostanin, A. Ernst, and I. Mertig. First-principles study of manganese-stabilized hafnia. *Journal of Magnetism and Magnetic Materials*, 321:913–916, 2009.

[81] M. Khalid, A. Setzer, M. Ziese, P. Esquinazi, D. Spemann, A. Pöppl, and E. Goering. Ubiquity of ferromagnetic signals in common diamagnetic oxide crystals. *Phys. Rev. B*, 81(21):214414, Jun 2010.

[82] G. Kresse, O. Dulub, and U. Diebold. Competing stabilization mechanism for the polar ZnO(0001)-Zn surface. *Phys. Rev. B*, 68(24):245409, Dec 2003.

[83] S Gallego, J I Beltrán, J Cerdá, and M C Muñoz. Magnetism and half-metallicity at the o surfaces of ceramic oxides. *Journal of Physics: Condensed Matter*, 17(43):L451, 2005.

[84] N. Sanchez, S. Gallego, and M. C. Muñoz. Magnetic states at the oxygen surfaces of ZnO and Co-doped ZnO. *Phys. Rev. Lett.*, 101(6):067206, 2008.

[85] N. Sanchez, S. Gallego, J. Cerdá, and M. C. Muñoz. Tuning surface metallicity and ferromagnetism by hydrogen adsorption at the polar zno(0001) surface. *Phys. Rev. B*, 81:115301, 2010.

[86] G. Fischer, N. Sanchez, W. Adeagbo, M. Lüders, Z. Szotek, W. M. Temmerman, A. Ernst, W. Hergert, and M. C. Muñoz. Room-temperature p-induced surface ferromagnetism: First-principles study. *Phys. Rev. B*, 84:205306, 2011.

[87] Alex Zunger, Stephan Lany, and Hannes Raebiger. The quest for dilute ferromagnetism in semiconductors: Guides and misguides by theory. *Physics*, 3:53, Jun 2010.

[88] A. Droghetti, C. D. Pemmaraju, and S. Sanvito. Predicting d^0 magnetism: Self-interaction correction scheme. *Phys. Rev. B*, 78(14):140404, Oct 2008.

[89] W. A. Adeagbo, G. Fischer, A. Ernst, and W. Hergert. Magnetic effects of defect pair formation in ZnO. *Journal of Physics: Condensed Matter*, 22(43):436002, 2010.

[90] H. L. Meyerheim, A. Ernst, K. Mohseni, I. V. Maznichenko, S. Ostanin, F. Klimenta, N. Jedrecy, W. Feng, I. Mertig, R. Felici, and J. Kirschner. batio$_3$(001)-(2h$bf\times$1): Surface structure and spin density. *Phys. Rev. Lett.*, 108:215502.